Discrete-Time-Model-Based Dynamic Decoupling Active Damping Current Control for CSI-Fed High-Speed PMSM With Low Carrier Ratio

Jindong Zhang, *Student Member, IEEE*, Fei Peng, *Member, IEEE*, Yunkai Huang, and Yu Yao, *Member, IEEE*

***Abstract*—This article proposes a dynamic decoupling active damping current control method for the current-source inverter (CSI)-fed high-speed permanent magnet synchronous machine (HSPMSM) drive with low carrier ratios. In this system, the natural resonance frequency is relatively high compared with the conventional CSI-fed system due to the high fundamental frequency and low inductance of the HSPMSM, which makes the traditional capacitor-voltage-feedback-based active damping fail. To achieve the desired resonance damping effects, the discrete-time-model-based multistate feedback active damping is proposed, which can configure the resonance pole arbitrarily. Then, to solve the serious cross coupling under low carrier ratios, a low-frequency-equivalent-transfer-function-based dynamic decoupling method is proposed for the parts where the traditional decoupling method cannot be applied. On the above basis, an outer-loop proportional–integral controller is adopted to adjust the magnitude and phase of the open-loop transfer function. In this way, the desired open-loop cutoff frequency with enough phase and gain margin can be achieved under the wide fundamental frequency changes of the HSPMSM. Finally, the effectiveness of the proposed method is verified by experiments.**

***Index Terms*—Active damping (AD), current control, current-source inverter (CSI), dynamic decoupling, high-speed permanent magnet synchronous machine (HSPMSM).**

I. Introduction

BENEFITING from the high-efficiency, high-power-density, and gearbox-free operation, high-speed permanent magnet synchronous machines (HSPMSMs) are widely used in engineering applications, such as air blowers, microturbine generators, and electric vehicles [1]. However, due to the high fundamental frequency (usually greater than 1000 Hz) and small stator inductance, the HSPMSM has large winding current ripples when fed by voltage-source inverters (VSIs) with limited switching frequencies. The large current ripples will increase the electromagnetic torque fluctuation, aggravate the vibration and noise [2], and bring additional losses to both the stator and the rotor [3]. The current-source inverter (CSI) is a favorable candidate for reducing the current ripple in the HSPMSM drive, benefiting from the inherent output filter capacitor. Also, the boost capability of the CSI can alleviate the voltage limitations of the VSI in high-speed operation, thus expanding the operating range and design freedom of the HSPMSM. In addition, the issues of high dv/dt and electromagnetic interference can be suppressed in the CSI-fed system [4], [5]. With these superiorities, the CSI-fed HSPMSM drive attracts more and more attention [6], [7].

In the configuration of the CSI, the filter capacitor is essential to buffer the pulsewidth modulation (PWM)-type CSI output current and the inductive load, resulting in the existence of LC connections. The LC resonance not only excites oscillations near the resonance frequency but also endangers the stability of the control system, which brings challenges to the control of the CSI-fed system. To solve this problem, resonance damping measures are necessary in the CSI-fed system. A simple and effective resonance damping solution is to insert passive resistors into the CSI filter network, which is so-called passive damping. However, inserted resistors cause additional power loss and reduce system efficiency. To avoid inserting the passive resistor, active damping (AD) strategies for CSI-fed systems are extensively researched in the literature. Generally, the AD is implemented in the inner loop of the control system, and an outer-loop controller is adopted for the control of load current. The existing AD methods are mainly based on the filter capacitor voltage feedback [8], [9], [10], [11], [12], [13], [14], [15], which achieves satisfactory resonance damping effects in permanent magnet synchronous machine (PMSM) drives [8], [9], [10], [11], [12] and grid-connected systems [13], [14], [15].

However, it is found in this article that the capacitor voltage feedback has a limited resonance damping effect in the CSI-fed HSPMSM system, which is quite different from the conventional CSI-fed system. Due to the high fundamental frequency and small stator inductance of the HSPMSM, the natural resonance frequency of the CSI-fed HSPMSM is relatively high compared to the conventional situation. In this case, the capacitor voltage feedback not only has a limited resonance damping effect

Manuscript received 5 October 2023; revised 20 December 2023 and 26 January 2024; accepted 28 February 2024. Date of publication 1 March 2024; date of current version 19 April 2024. This work was supported by the National Natural Science Foundation of China under Grant 52277036 and Grant 52277037. Recommended for publication by Associate Editor M. Hartmann. *(Corresponding author: Fei Peng.)*

The authors are with the School of Electrical Engineering, Southeast University, Nanjing 210018, China (e-mail: 21st@seu.edu.cn; pengfei@seu.edu.cn; huangyk@seu.edu.cn; yuyao@seu.edu.cn).

Color versions of one or more figures in this article are available at https://doi.org/10.1109/TPEL.2024.3372198.

Digital Object Identifier 10.1109/TPEL.2024.3372198

but may even make the plant unstable. Theoretical analysis shows that in this case, the capacitor-voltage- and load-current-feedback-based multistate feedback active damping (MSFAD) is required to obtain satisfactory damping effects. In [16], the damping effects of various state feedback in the CSI-fed system have been exhaustively analyzed and discussed, including the capacitor voltage, capacitor current, load voltage, and load current. However, this work is based on the continuous-time model and does not take into account digital and PWM delays. In the HSPMSM drive, the carrier ratio (namely, the ratio of sampling frequency to fundamental frequency) is relatively small due to the high fundamental frequency. Under the low carrier ratio, the accuracy of the continuous-time model decreases because of the discretization approximation, and the discrete-time model needs to be adopted to obtain the expected control performance [17]. The series virtual resistor proposed in [18] essentially uses the capacitor voltage and load current multistate feedback to dampen the resonance. However, although the stability of this method is rigorously proven in the discrete domain, the design process is still based on the continuous-time model. In the authors' previous work [19], a pole-placement-based current control method using the motor current feedback is proposed in the CSI-fed PMSM system. However, this method is not suitable for high-speed applications since the high fundamental frequency and the dynamic decoupling problem are not considered. To obtain the desired AD performance in the CSI-fed HSPMSM system, the discrete-time-model-based MSFAD needs to be further studied.

In the low-carrier-ratio case, another challenge is the serious cross coupling in the dq synchronous frame. The reason for cross coupling can be explained by the dq transform causing a nonzero imaginary part in the system transfer function [20], and the amplitude of the imaginary part will increase as the carrier ratio decreases, which leads to more serious cross coupling. State feedforward is a commonly used decoupling method [8], [18], [21], which aims to directly compensate for cross-coupling terms. However, the feedforward accuracy decreases in the low-carrier-ratio case because of the increased system delay. Adopting a complex controller to cancel the imaginary part of the plant, which can be noted as the direct cancellation method, is an effective decoupling method in the VSI-fed system [22], [23], [24], and it is proven to be effective even at low carrier ratios [24]. However, theoretical analysis shows that the direct cancellation method can only solve part of the cross-coupling problem in the CSI-fed system. In [10], dynamic decoupling is achieved through a combination of state feedforward and complex coefficient compensation in the CSI-fed PMSM system with low carrier ratios. However, this method is not guaranteed to be suitable for high-speed ranges, since it is not designed for high-speed motor applications.

To solve the above problems, this article proposes a discrete-time-model-based dynamic decoupling AD current control method for the CSI-fed HSPMSM drive with low carrier ratios. The contributions of this work mainly lie in the following two aspects.

1) The MSFAD utilizing the capacitor voltage and motor current feedback are studied based on the discrete-time model. Theoretical analysis shows that the position of the resonance pole pair can be configured arbitrarily through the MSFAD, which means that the desired resonance frequency and damping ratio can be achieved. This is better than single-state-feedback-based AD that can only select the resonance pole position on a single locus.
2) Theoretical analysis shows that the signal flow of the dq-frame-based open-loop transfer function is mainly in the low-frequency band. On this basis, a low-frequency equivalent transfer function (LFETF)-based dynamic decoupling method is proposed to solve the cross-coupling problem of the plant after MSFAD.

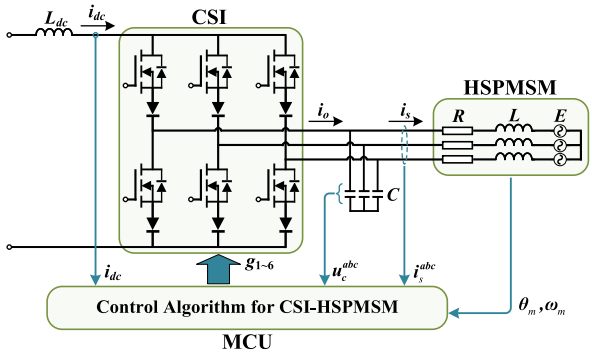

Fig. 1. Diagram of the CSI-fed HSPMSM drive.

On the above basis, an outer-loop proportional–integral (PI) controller is adopted to adjust the magnitude and phase of the open-loop transfer function. In this way, the desired open-loop cutoff frequency with enough phase margin (PM) and gain margin (GM) can be achieved under the wide fundamental frequency changes of the HSPMSM, which ensures the dynamic performance, stability, and robustness of the system. The effectiveness of the proposed method is verified by the experiments on a CSI-fed HSPMSM drive with the fundamental frequency 1000 Hz.

The rest of this article is organized as follows. In Section II, the discrete-time model of the CSI-fed HSPMSM is developed, and the resonance phenomenon is analyzed. In Section III, the limits of the single-state-feedback-based AD are demonstrated, and the discrete-time-model-based MSFAD is proposed. Section IV analyzes the frequency spectrum of the open-loop transfer function signal flow and proposes the LFETF-based dynamic decoupling controller. Section V completes the design of the open-loop Bode plot and evaluates the robustness of the control system. In Section VI, the experimental results are presented to verify the effectiveness of the proposed method. Finally, Section VII concludes this article.

II. Modeling and Resonance Analysis of the CSI-Fed HSPMSM System

A. Discrete-Time Model of the CSI-Fed HSPMSM

Fig. 1 shows the diagram of the CSI-fed HSPMSM drive. $i_{\rm dc}$ is the dc bus current, and $L_{\rm dc}$ is the dc bus inductance. C is the filter capacitor, R is the motor resistance, and L is the motor

inductance. i_o is the CSI output current, i_s is the motor current, u_c is the filter capacitor voltage, and E is the back electromotive force (EMF) of the HSPMSM. θ_m and ω_m are the rotor position and speed, respectively.

Since the high-speed PMSM has a limited number of coil turns, the motor resistance is relatively small, and there is $R \ll \omega_e L$ in high-speed operation (ω_e is the motor electrical angular speed). Accordingly, the motor resistance can be ignored in the modeling. Also, it is noted that the resistance is the inherent damping of the system, so ignoring resistance, namely, considering $R = 0$, represents the most severe case of resonance. Thus, ignoring resistance during control design does not endanger the system stability, which will be verified in Section V-B. On the other hand, since the mechanical dynamic is much slower than the electrical dynamic, the back EMF is considered a slow-changing disturbance and can be automatically compensated by the controller. Therefore, the back EMF is also ignored in the modeling. On the above basis, the continuous-time transfer functions from CSI output current i_o to motor current i_s and to filter capacitor voltage u_c are derived as

$$G_{is}(s) = \frac{I_s^{\alpha\beta}(s)}{I_o^{\alpha\beta}(s)} \approx \frac{\omega_r^2}{s^2 + \omega_r^2} \tag{1}$$

$$G_{uc}(s) = \frac{U_c^{\alpha\beta}(s)}{I_o^{\alpha\beta}(s)} \approx \frac{L\omega_r^2 s}{s^2 + \omega_r^2} \tag{2}$$

where

$$\omega_r = \frac{1}{\sqrt{LC}} \tag{3}$$

is the natural resonance frequency; $I_s^{\alpha\beta} = I_s^{\alpha} + jI_s^{\beta}$, $I_o^{\alpha\beta} = I_o^{\alpha} + jI_o^{\beta}$, and $U_c^{\alpha\beta} = U_c^{\alpha} + jU_c^{\beta}$ are the corresponding complex variables in the frequency domain.

To ensure the model accuracy under low carrier ratios, it is necessary to develop the discrete-time model. The PWM-type CSI output current i_o is considered average within one sampling period, so the discrete-time transfer functions can be derived by the zero-order-hold discretization method as

$$G_{is}(z) = \frac{z-1}{z} \cdot \mathcal{Z}\left\{\frac{G_{is}(s)}{s}\right\} = \eta \frac{z+1}{z^2 - 2\cos(\omega_r T)z + 1} \tag{4}$$

$$G_{uc}(z) = \frac{z-1}{z} \cdot \mathcal{Z}\left\{\frac{G_{uc}(s)}{s}\right\} = \mu \frac{z-1}{z^2 - 2\cos(\omega_r T) + 1} \tag{5}$$

with

$$\eta = 1 - \cos(\omega_r T),\ \mu = \sqrt{\frac{L}{C}}\sin(\omega_r T) \tag{6}$$

where $\mathcal{Z}\{\cdot\}$ is the z-transform and T is the sampling period.

In practice, since the signal sampling and control algorithm running takes a certain amount of time, there is a one-step digital delay in the PWM duty update. Therefore, the plant transfer function considering the motor current as the control target is

$$G_p(z) = z^{-1}G_{is}(z) = \frac{\eta(z+1)}{z\,(z^2 - 2\cos(\omega_r T)z + 1)}$$

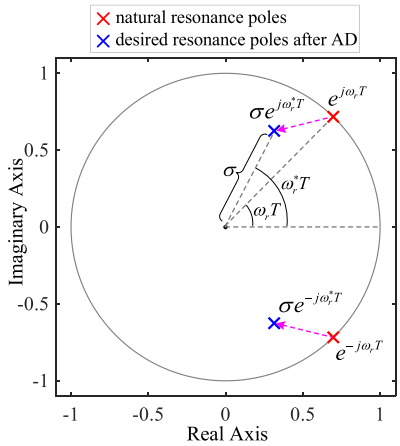

Fig. 2. Resonance pole pair of the CSI-fed system.

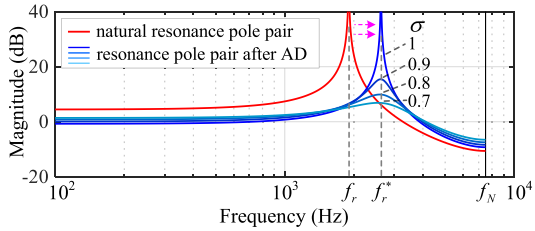

Fig. 3. Bode plot of the resonance pole pair.

$$= \frac{\eta(z+1)}{z(z - e^{j\omega_r T})(z - e^{-j\omega_r T})}. \tag{7}$$

B. Resonance Analysis

According to (7), there is a natural resonance pole pair $e^{\pm j\omega_r T}$ with the resonance frequency ω_r and modulus 1, as shown by the red poles in Fig. 2. (When considering the system resistance, the modulus of the resonance pole is slightly less than 1.) The natural pole pair causes the transfer function to have large amplitudes near the resonance frequency, as shown by the red Bode plot in Fig. 3 ($2\pi f_r = \omega_r$, f_N is the Nyquist frequency). The towering resonance peak not only excites oscillations near the resonance frequency but also endangers the stability of the control system.

To solve the resonance problems, the AD needs to be implemented to change the position of the resonance pole pair. The purpose of AD is to achieve the desired resonance frequency f_r^* and modulus σ, that is, to change the resonance pole pair to $\sigma e^{\pm j\omega_r^* T}$ ($\omega_r^* = 2\pi f_r^*$), as shown by the blue poles in Fig. 2. The resonance frequency f_r^* is desired to increase to avoid low-order harmonics exciting the resonance. Also, the high resonance frequency makes the resonance peak far away from the low-frequency band, which is closely related to system stability, and is thus beneficial to the design of the control system. On the other hand, the modulus of resonance pole σ is desired to decrease to weaken the resonance peak, as shown by the blue Bode plot in Fig. 3. Therefore, taking the resonance pole in the upper half-plane as an example, it is hoped that AD can make the resonance pole move counterclockwise and toward the origin, as shown by the magenta dashed line in Fig. 2.

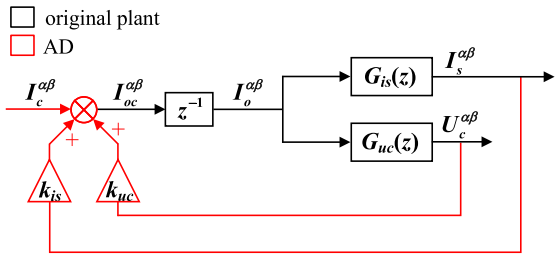

Fig. 4. Control diagram of AD when considering the capacitor voltage and motor current feedback.

III. Discrete-Time-Model-Based MSFAD Utilizing the Capacitor Voltage and Motor Current Feedback

Generally, the AD is based on the capacitor voltage feedback in CSI-fed systems [8], [10], [13], [14], [15]. However, it is found that the capacitor voltage feedback has a limited resonance damping effect in the CSI-fed HSPMSM system. This is because the natural resonance frequency of the CSI-fed HSPMSM is relatively high compared with that of the conventional CSI-fed system. This section will first analyze the above issues and then propose the discrete-time-model-based MSFAD to achieve the desired resonance damping effect under low carrier ratios.

Considering the capacitor voltage and motor current feedback, the control block diagram of the inner-loop AD is shown in Fig. 4, where k_{uc} and k_{is} are, respectively, the capacitor voltage and motor current feedback coefficients, $I_c^{\alpha\beta}$ is the outer-loop controller output, and $I_{oc}^{\alpha\beta}$ is the CSI output current reference generated by the overall control strategy. According to Fig. 4, the transfer function of the plant after AD is

$$G_{in}^{\alpha\beta}(z)=\frac{I_s^{\alpha\beta}}{I_c^{\alpha\beta}}=\frac{z^{-1}G_{is}(z)}{1-k_{uc}z^{-1}G_{uc}(z)-k_{is}z^{-1}G_{is}(z)}. \quad (8)$$

Since the AD does not need to be implemented in the dq synchronous frame, the analysis in this section is all based on the $\alpha\beta$ stationary frame.

A. Resonance Damping Effects of the Single-State Feedback

This subsection demonstrates the different resonance damping effects of single-state feedback (capacitor voltage or motor current) in the conventional CSI-fed system and the CSI-fed HSPMSM system. In [8], the capacitor voltage feedback is adopted to achieve resonance damping in a conventional CSI-fed PMSM drive. This system serves as an example of the conventional CSI-fed system here, and the parameters are switching frequency $f_{\text{sw}}=16$ kHz, sampling frequency $f_s=32$ kHz, $L=2$ mH, $C=10$ μF, and $f_r=1.13$ kHz [8]. It can be seen that the natural frequency resonance f_r is designed to be significantly lower than the switching frequency f_{sw} in order to filter out the switching frequency harmonics. Note that the ratio of natural resonance frequency to sampling frequency is $r_1=f_r/f_s=0.035$.

Fig. 5 shows the resonance pole locus when using 1) capacitor-voltage-feedback-based or 2) motor-current-feedback-based AD, which are calculated through (8). It can be seen from

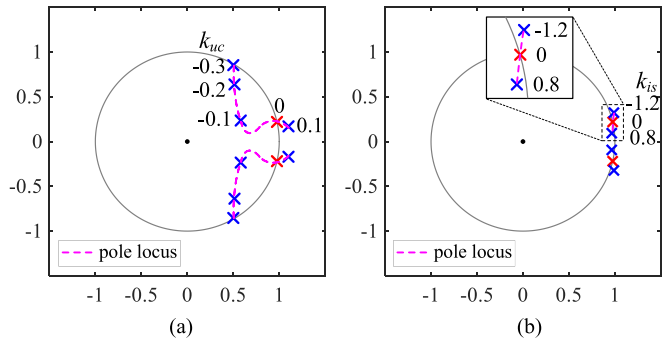

Fig. 5. Resonance pole locus when using the single-state feedback based AD in the conventional CSI-fed PMSM system [8]. (a) Capacitor voltage feedback. (b) Motor current feedback.

Fig. 5(a) that, compared with the natural resonance pole marked in red, the resonance pole meets the requirements of resonance frequency increase and modulus decrease when $k_{uc}\in[-0.2,-0.1]$. This indicates that the resonance damping effect is good within this range, which is consistent with the results in [8]. On the other hand, it is obvious from Fig. 5(b) that the motor current feedback has no resonance damping effect in this case.

Different from the conventional PMSM, the HSPMSM has the characteristics of high fundamental frequency and small inductance, which prevents the CSI-fed HSPMSM from designing the natural resonance frequency in a lower range like conventional CSI-fed systems. First, if the natural resonance frequency is low, the high fundamental frequency of the HSPMSM will excite system resonance and make the system unstable. Also, since the inductance of the HSPMSM is small and the natural resonance frequency $\omega_r=1/\sqrt{LC}$, achieving a small resonance frequency requires larger filter capacitance, which increases system size and cost and reduces efficiency. On the other hand, larger filter capacitance also requires more reactive current, which can be derived as

$$i_{c,E}^d=-\frac{\omega_e E}{L(\omega_r^2-\omega_e^2)} \quad (9)$$

where $i_{c,E}^d$ represents the capacitor current required to maintain the capacitor voltage that counteracts the back EMF E. Note that this capacitor current is in the direction of the negative d-axis, which is orthogonal to the motor active current in the direction of the q-axis. In the HSPMSM, ω_e is high and L is small, so CSI-fed HSPMSM systems require much more capacitor current than ordinary CSI-fed PMSM systems. It can be seen from (9) that $i_{c,E}^d$ is larger when ω_r is lower, namely, when C is larger. Large $i_{c,E}^d$ increases the loss of the capacitor and increases the capacity requirements. Also, since $i_{c,E}^d$ is supplied by the CSI, large $i_{c,E}^d$ requires an increase in the dc-side current level, thereby increasing system losses and possibly exceeding the rated current of the dc inductor.

Based on the above discussion, it should select smaller filter capacitors on the premise that the switching harmonic filtering capability is sufficient. Specifically, the theoretical total harmonic distortion (THD) of motor current under rated

TABLE I
PARAMETERS OF THE TESTED CSI-FED HSPMSM DRIVE

Symbol	Parameter	Value
$f_{\rm sw}$	CSI average switching frequency	10 kHz
f_s	CSI sampling frequency (five-segment support vector machine)	15 kHz
T	CSI sampling period	66.7 μs
$L_{\rm dc}$	Inductance of the dc-link choke	6 mH
n_N	HSPMSM rated speed	12000 r/min
p	HSPMSM pole pairs	5
$f_{e,N}$	HSPMSM rated fundamental frequency	1000 Hz
ξ	Rated carrier ratio $f_s/f_{e,N}$	15
Ψ	HSPMSM permanent magnet flux linkage	0.026 Wb
R	HSPMSM phase resistance	0.3 Ω
L	HSPMSM phase inductance	400 μH
C	Filter capacitance	8 μF
f_r	Natural resonance frequency	2814 Hz

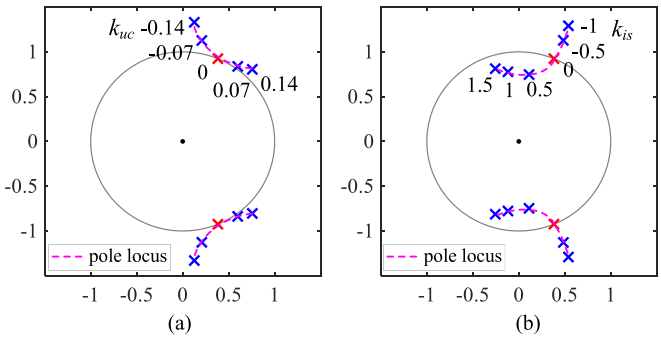

Fig. 6. Resonance pole locus when using the single-state-feedback-based AD in the CSI-fed HSPMSM system. (a) Capacitor voltage feedback. (b) Motor current feedback.

operating conditions should be less than 5%. It is obtained through the system simulation in MATLAB/Simulink that the THD $= 3.69\% < 5\%$ under $C = 8$ μF; thus, C is selected to 8 μF in the tested CSI-fed HSPMSM system. The other parameters are fundamental frequency $f_e = 1$ kHz, $f_s = 15$ kHz, and $L = 400$ μH, as listed in Table I. Therefore, $f_r = 2814$ Hz and the ratio of f_r to f_s is $r_2 = 0.187$, which is obviously higher than $r_1 = 0.035$ of the aforementioned conventional CSI-fed PMSM. In this case, the resonance pole locus when using 1) capacitor-voltage-feedback-based or 2) motor-current-feedback-based AD is shown in Fig. 6. Comparing Figs. 5(a) and 6(a), it is obvious that the resonance damping effect of the capacitor voltage feedback is very different in the conventional CSI-fed system and the CSI-fed HSPMSM. Actually, it can be seen from Fig. 6(a) that the capacitor voltage feedback not only has no damping effect but also makes the resonance pole unstable. Therefore, the existing capacitor-voltage-feedback-based AD cannot be used for the CSI-fed HSPMSM drive.

On the other hand, it can be seen from Fig. 6(b) that the motor current positive feedback has a certain resonance damping effect, which increases the resonance frequency and decreases the modulus. However, different CSI-fed PMSM applications have different ratio r of the natural resonance frequency to the sampling frequency, namely, have different resonance pole loci when using the single-state feedback. This means that even if there is a desired AD effect at a certain r, there is no guarantee that it will still be effective when r changes. To ensure that the desired AD effects can be achieved and thus the stable control system can be obtained, the next subsection will study the MSFAD based on the capacitor voltage and motor current feedback.

B. Discrete-Time-Model-Based MSFAD Utilizing the Capacitor Voltage and Motor Current Feedback

The AD utilizing multistate feedback in CSI-fed systems has been discussed in [16] and [18]. However, these works are based on the continuous-time model. In this article, the MSFAD will be analyzed based on the discrete-time model in order to be applied to the CSI-fed HSPMSM with low carrier ratios.

Substituting (4) and (5) into (8) gives

$$G_{in}^{\alpha\beta}(z) = \frac{\eta(z+1)}{z^3+\gamma_2 z^2+\gamma_1 z+\gamma_0} \triangleq \frac{N(z)}{D(z)} \tag{10}$$

where

$$\begin{cases} \gamma_2 = -2\cos(\omega_r T) \\ \gamma_1 = -\mu k_{uc} - \eta k_{is} + 1 \\ \gamma_0 = \mu k_{uc} - \eta k_{is}. \end{cases} \tag{11}$$

The order of the denominator polynomial $D(z)$ is 3, and the polynomial coefficients can be configured through the feedback coefficients k_{uc} and k_{is}, as shown in (11).

Similar to the denominator of the original plant (7), it can be assumed that $D(z)$ contains a resonance pole pair and a real pole. Accordingly, the desired $D(z)$ is designed as

$$\begin{aligned} D^*(z) &= (z-p)\left(z^2 - 2\sigma\cos(\omega_r^* T)z + \sigma^2\right) \\ &= (z-p)(z-\sigma e^{j\omega_r^* T})(z-\sigma e^{-j\omega_r^* T}) \end{aligned} \tag{12}$$

where $\sigma e^{\pm j\omega_r^* T}$ is the desired resonance pole pair, ω_r^* is the desired resonance frequency, σ is the desired modulus, and p is the real pole. Equation (12) can be further written in polynomial form as

$$D^*(z) \triangleq z^3 + \gamma_2^* z^2 + \gamma_1^* z + \gamma_0^* \tag{13}$$

with

$$\begin{cases} \gamma_2^* = -p - 2\sigma\cos(\omega_r^* T) \\ \gamma_1^* = \sigma^2 + 2p\sigma\cos(\omega_r^* T) \\ \gamma_0^* = -p\sigma^2. \end{cases} \tag{14}$$

Let $\gamma_j = \gamma_j^*, j = 2, 1, 0$; it can be obtained through mathematical operations that

$$k_{uc} = \frac{1}{2\mu}\left\{\begin{array}{c} 2\sigma^3\cos(\omega_r^* T) - 4\sigma\cos^2(\omega_r^* T)\cos(\omega_r T) + 1 \\ +\sigma^2\left(4\cos^2(\omega_r^* T) - 2\cos(\omega_r T) - 1\right) \end{array}\right\} \tag{15}$$

$$k_{is} = \frac{1}{2\eta}\left\{\begin{array}{c} -2\sigma^3\cos(\omega_r^* T) - 4\sigma\cos^2(\omega_r^* T)\cos(\omega_r T) + 1 \\ +\sigma^2\left(4\cos^2(\omega_r^* T) + 2\cos(\omega_r T) - 1\right) \end{array}\right\} \tag{16}$$

$$p = 2\left(\cos(\omega_r T) - \sigma\cos(\omega_r^* T)\right). \tag{17}$$

Based on (15) and (16), it can be seen that, for any desired resonance frequency ω_r^* and modulus σ, the corresponding feedback coefficients k_{uc} and k_{is} can be obtained. Therefore,

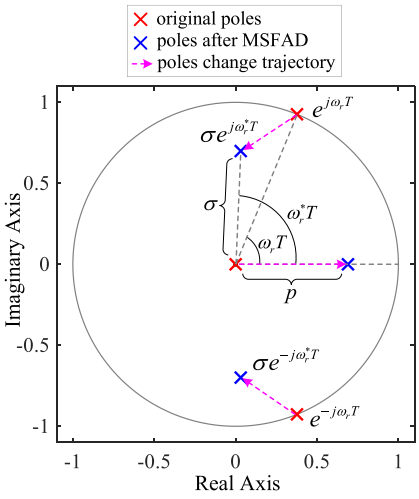

Fig. 7. Poles of the original plant $G_p(z)$ and the plant after MSFAD $G_{in}^{\alpha\beta}(z)$.

the resonance pole position can be configured arbitrarily by the MSFAD, which is not restricted by the ratio r of the natural resonance frequency to the sampling frequency. This is better than single-state-feedback-based AD that can only select the resonance pole position on a single locus that depends on r, as shown in Figs. 5 and 6.

On the other hand, (17) shows the position of the real pole p in the plant after MSFAD $G_{in}^{\alpha\beta}(z)$, and it is obvious that p is related to the desired resonance pole $\sigma e^{\pm\omega_r^* T}$. It is noted that $G_{in}^{\alpha\beta}(z)$ should be stable, which requires that the real pole p is less than 1. As discussed in Section II-B, we hope that the desired resonance frequency ω_r^* increases and the desired modulus σ decreases, which mean $\cos(\omega_r^* T) < \cos(\omega_r T)$ and $\sigma < 1$. To ensure that $p < 1$, it can be seen from (17) that the increase in ω_r^* and the decrease in σ cannot be excessive. Considering the possible pole shift due to the system error, it is recommended to guarantee that

$$p \leqslant 0.95 \tag{18}$$

which will be analyzed in the next subsection.

Substituting (18) into (17), it can be derived that ω_r^* and σ should satisfy

$$\sigma \cos(\omega_r^* T) \geqslant \cos(\omega_r T) - 0.475. \tag{19}$$

Limited by (19), the recommended parameter selection in this case is

$$\omega_r^* = \omega_r + \frac{\omega_N}{10}, \quad \sigma = 0.7 \tag{20}$$

where ω_N is the Nyquist frequency. In the tested CSI-fed HSPMSM system, the desired resonance frequency is $\omega_r^* = (2814 + 750) \times 2\pi = 3564 \times 2\pi$ rad/s according to (20).

The plant after the MSFAD is

$$G_{in}^{\alpha\beta}(z) = \frac{I_s^{\alpha\beta}}{I_c^{\alpha\beta}} = \frac{\eta(z+1)}{(z-p)(z-\sigma e^{j\omega_r^* T})(z-\sigma e^{-j\omega_r^* T})}. \tag{21}$$

The poles of the original plant $G_p(z)$ (in red) and $G_{in}^{\alpha\beta}(z)$ (in blue) are shown in Fig. 7. It can be seen that the resonance pole

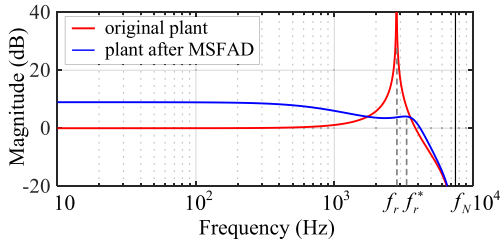

Fig. 8. Bode plot of the original plant $G_p(z)$ and the plant after MSFAD $G_{in}^{\alpha\beta}(z)$.

pair is moved from $e^{\pm j\omega_r T}$ to $\sigma e^{\pm j\omega_r^* T}$, and the pole at the origin is moved to p. The Bode plots of $G_p(z)$ (in red) and $G_{in}^{\alpha\beta}(z)$ (in blue) are shown in Fig. 8. Obviously, the resonance frequency is increased, and the resonance peak is suppressed through the MSFAD, which are consistent with design expectations.

It should be noted that the purpose of this subsection is to give the discrete analytical expressions of the MSFAD inner loop, as shown in (15)–(17), and (21), which are the basis for the subsequent design of the decoupling controller in Section IV and the current controller in Section V.

In this article, the AD effect is observed through the position of the resonance pole. In addition, it is well known that the AD effect of state feedback can be understood as the virtual impedance. When considering the 1.5-beat control delay, the capacitor voltage negative feedback can emulate the virtual resistor in parallel with the filter capacitor when $\cos(1.5\omega_r T) > 0$ or $f_r/f_s < 1/6$ [8], and the motor inductor current positive feedback can emulate the virtual capacitor in series with the inductor when $\sin(1.5\omega_r T) > 0$ or $f_r/f_s < 1/3$. However, the resonance frequency f_r is relatively high in the CSI-fed HSPMSM, and the ratio is $f_r/f_s = 0.187 > 1/6$, which exceeds the effective range of the capacitor-voltage-negative-feedback-based virtual resistor. This can be indicated by Fig. 6(a), where the capacitor voltage feedback cannot move the resonance pole into the unit circle and bring active damping effects. Although the ratio $f_r/f_s = 0.187$ is in the effective range of the inductor-current-positive-feedback-based virtual capacitor, it is still difficult to ensure the desired active damping effects only using the inductor current feedback. In comparison, the proposed multistate feedback can ensure the desired AD effects and is not restricted by f_r/f_s, which is more suitable for the CSI-fed HSPMSM system.

In addition to the proportional-feedback-based AD discussed in this section, there is filter-feedback-based AD in the CSI or current source rectifier (CSR) system [14], [25], [26], which can also achieve AD effects with reasonable parameter selection principles. However, the feedback order of filter-based AD is greater than or equal to 1, and thus, the order of the corresponding AD inner loop will increase. This will increase the difficulty of the dynamic decoupling in the outer loop, so is undesirable in the CSI-fed HSPMSM with low carrier ratios. By contrast, the multistate proportional feedback proposed in this article will not increase the order of the inner-loop transfer function, which is shown by the comparison between the original plant (7) and the plant after MSFAD (21). Therefore, the proportional feedback

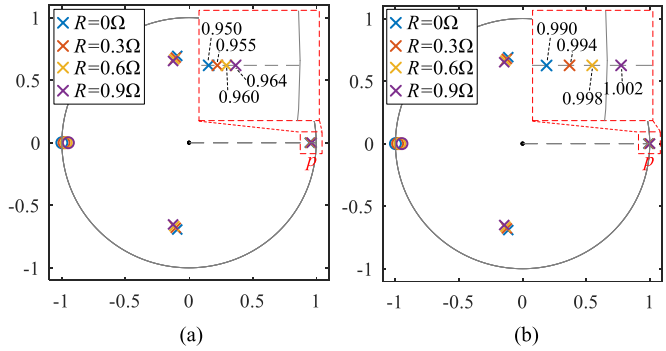

Fig. 9. Zero and pole of the plant after MSFAD $G_{in}^{\alpha\beta}(z)$ when the actual parameter R changes. (a) $p = 0.95$. (b) $p = 0.99$.

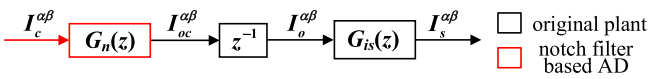

Fig. 10. Control diagram of the notch-filter-based AD.

is more recommended than the filter feedback to achieve AD in the CSI-fed HSPMSM.

C. Analysis of the Selection Principle of p in (18)

Fig. 9 shows the zero and pole of the plant after MSFAD $G_{in}^{\alpha\beta}(z)$ when the actual parameter R changes. It can be verified that the error of L and C hardly causes p to shift, so it is not discussed. R presents the actual resistance value and is adopted in the system model. Note that the motor resistance normal value is $R_{\text{norm}} = 0.3\ \Omega$, which is listed in Table I. However, the actual value of the resistance is likely to increase due to cable resistance, terminal resistance, temperature rise, and the skin effect of high-frequency motors. Therefore, the set actual resistance R in Fig. 9 is up to $0.9\ \Omega$ $(= 3R_{\text{norm}})$. It can be seen from Fig. 9(a) that, when p is set to 0.95, p has a certain shift as R increases from 0 to $0.9\ \Omega$, but it is still inside the unit circle. However, it is observed from Fig. 9(b) that, when p is set to 0.99, p shifts outside the unit circle as R increases from 0 to $0.9\ \Omega$, which means that the stability of the control system will be affected. The above analysis indicates that setting p too close to 1 will affect system stability under the parameter error, and $p \leqslant 0.95$ is a reliable condition for maintaining stability.

D. Comparative Analysis Between the MSFAD and the Notch-Filter-Based AD

Fig. 10 shows the control diagram of the notch-filter-based AD, which is expected to use the notch filter to cancel the resonance peak of the original plant [27]. The transfer function of the notch filter is as follows [28]:

$$G_n(z) = \frac{(1+\eta_2)z^2 - 2\eta_1 z + (1+\eta_2)}{2(z^2 - \eta_1 z + \eta_2)}. \tag{22}$$

Coefficients η_1 and η_2 are expressed as

$$\eta_1 = \frac{2\cos(\omega_0 T)}{1+\tan(\frac{\Omega T}{2})},\ \eta_2 = \frac{1-\tan(\frac{\Omega T}{2})}{1+\tan(\frac{\Omega T}{2})} \tag{23}$$

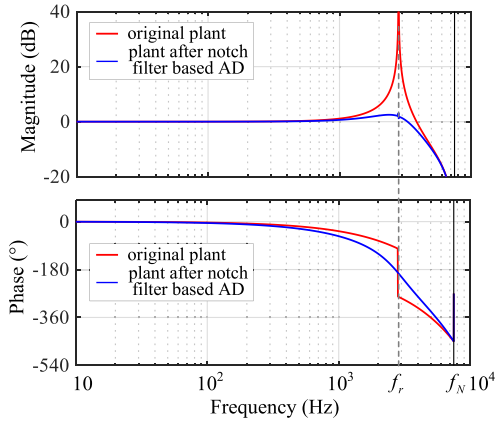

Fig. 11. Bode plot of the original plant $G_p(z)$ and the plant after the notch-filter-based AD with accurate parameters.

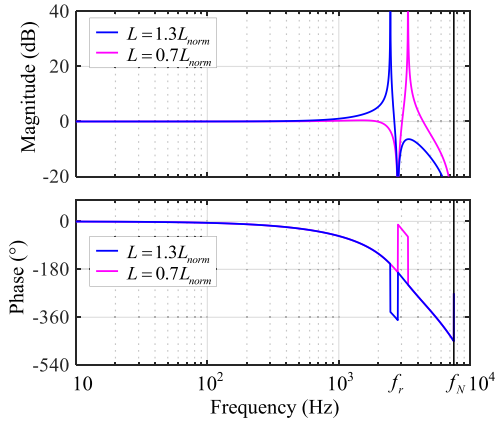

Fig. 12. Bode plot of the plant after the notch-filter-based AD with ±30% error of motor inductance L.

where ω_0 is the notch frequency and Ω is the 3-dB rejection bandwidth. In this study, ω_0 is set to the natural resonance frequency $2814 \times 2\pi$ rad/s, Ω is set to $2000 \times 2\pi$ rad/s.

Fig. 11 shows the Bode plot of the original plant (red) and the plant after the notch-filter-based AD with accurate parameters (blue). It can be seen that the resonance peak is well dampened when the parameters are accurate. However, Fig. 12 shows the Bode plot with ±30% error of motor inductance L, where L_{norm} is the normal inductance adopted in the controller, and L is the actual inductance adopted in the system model. It is shown that the resonance peak cannot be dampened under the parameter error, which indicates that the parameter robustness of the notch-filter-based AD is poor. In contrast, Fig. 13 shows the Bode plot of the plant after the MSFAD with ±30% error of motor inductance L. It can be seen that the resonance peak is still well dampened despite the parameter error. The above comparisons demonstrate that the robustness of the proposed MSFAD is significantly better than the notch-filter-based AD.

IV. LFETF-Based Dynamic Decoupling Controller

In order to achieve high-performance current control under a wide range of fundamental frequency changes, the outer-loop

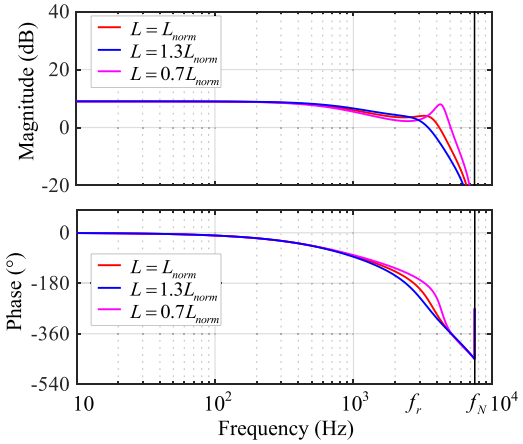

Fig. 13. Bode plot of the plant after the MSFAD with ±30% error of motor inductance L.

current controller should be developed in the dq synchronous frame. For the convenience of discussion, the inner-loop transfer function after MSFAD $G_{in}^{\alpha\beta}(z)$ is divided into three parts

$$G_{in}^{\alpha\beta}(z)=\eta\cdot\underbrace{\frac{1}{(z-p)}}_{G_{in1}^{\alpha\beta}}\cdot\underbrace{(z+1)}_{G_{in2}^{\alpha\beta}}\cdot\underbrace{\frac{1}{(z-\sigma e^{j\omega_r^* T})(z-\sigma e^{-j\omega_r^* T})}}_{G_{in3}^{\alpha\beta}}. \tag{24}$$

Substituting $ze^{j\omega_e T}$ for z into (24) gives the transfer function in the dq frame [10]

$$G_{in}^{dq}(z)=\eta\cdot\underbrace{\frac{1}{(ze^{j\omega_e T}-p)}}_{G_{in1}^{dq}}\cdot\underbrace{(ze^{j\omega_e T}+1)}_{G_{in2}^{dq}}\cdot\underbrace{\frac{1}{(ze^{j\omega_e T}-\sigma e^{j\omega_r^* T})(ze^{j\omega_e T}-\sigma e^{-j\omega_r^* T})}}_{G_{in3}^{dq}}. \tag{25}$$

It can be seen from (25) that the dq transformation causes the complex term $e^{j\omega_e T}=\cos(\omega_e T)+j\sin(\omega_e T)$ to appear in the transfer function, which results in a nonzero imaginary part of the transfer function, namely, $G_{in}^{dq}=G_{in,r}^{dq}+jG_{in,i}^{dq}$. In this case, the input excitation of the d-axis or q-axis will not only cause responses in this axis but also cause responses in the other axis, that is, the cross-coupling phenomenon [20]. As the fundamental frequency f_e increases, the carrier ratio of the control system $\xi=f_s/f_e$ decreases, and the imaginary part of the complex term $j\sin(\omega_e T)=j\sin(2\pi/\xi)$ increases, thereby aggravating the cross coupling. At low carrier ratios, cross coupling seriously affects the dynamic performance and stability of the system, and effective dynamic decoupling measures are necessary to be taken.

According to (25), G_{in1}^{dq} can be decoupled by the direct cancellation method [22], [23], [24], and the corresponding dynamic decoupling controller is

$$G_{dd1}(z)=\frac{ze^{j\omega_e T}-p}{z-p_1}. \tag{26}$$

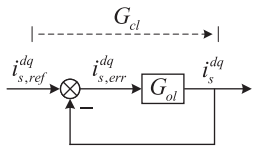

Fig. 14. Diagram of the closed-loop control system in the dq frame.

The transfer function after dynamic decoupling is

$$G_{a1}=G_{dd1}\cdot G_{in1}^{dq}=\frac{1}{z-p_1}. \tag{27}$$

Since the complex term is canceled, dynamic decoupling is achieved. It is noted that the denominator term $(z-p_1)$ of G_{dd1} is used to ensure that the denominator order of G_{dd1} is not lower than the numerator order, thereby ensuring its realizability.

However, the direct cancellation method does not apply to the remaining parts G_{in2}^{dq} and G_{in3}^{dq}. G_{in2}^{dq} corresponds to a negative unit zero. If a negative unit pole is used to cancel G_{in2}^{dq}, it will cause an oscillation component in the controller output thus making the control system unstable. G_{in3}^{dq} corresponds to the resonance pole pair, and directly canceling it requires high parameter accuracy. Also, if a second-order numerator is used to cancel the resonant pole pair, a suitable second-order denominator is also needed to meet the realizability requirement, which increases the complexity of the controller design.

In this section, an LFETF-based dynamic decoupling method is proposed for G_{in2}^{dq} and G_{in3}^{dq}. The next subsection will first explain that the signal flow of the dq-frame-based open-loop transfer function is mainly in the low-frequency band.

A. Frequency Analysis of Open-Loop Transfer Function Signal Flow

Fig. 14 shows the diagram of the closed-loop control system in the dq frame, where $G_{\rm ol}$ is the open-loop transfer function and $G_{\rm cl}$ is the closed-loop transfer function. Assuming that the control system has been properly designed, the unit step response of the motor current i_s^{dq} can be approximated as the negative exponential type, as shown by the red waveform in Fig. 15(a), namely

$$i_s^{dq}(t)=(1-e^{-at})\varepsilon(t) \tag{28}$$

where $\varepsilon(t)$ is the unit step function. Therefore, the open-loop transfer function input $i_{s,\rm err}^{dq}$ is

$$i_{s,\rm err}^{dq}(t)=e^{-at}\varepsilon(t) \tag{29}$$

as shown by the blue waveform in Fig. 15(a). Assume that the motor current reaches 90% of the step response reference value at the tenth sampling period T, i.e.,

$$i_s^{dq}(10T)=1-e^{-a\times 10T}=0.9\ \Rightarrow\ a=-\frac{\ln 0.1}{10T}. \tag{30}$$

In this study, the sampling frequency $f_s=15$ kHz; thus, $a\approx 3454$ according to (30). Then, based on the Fourier transform, the frequency spectrum of the open-loop input signal $i_{s,\rm err}^{dq}$ can

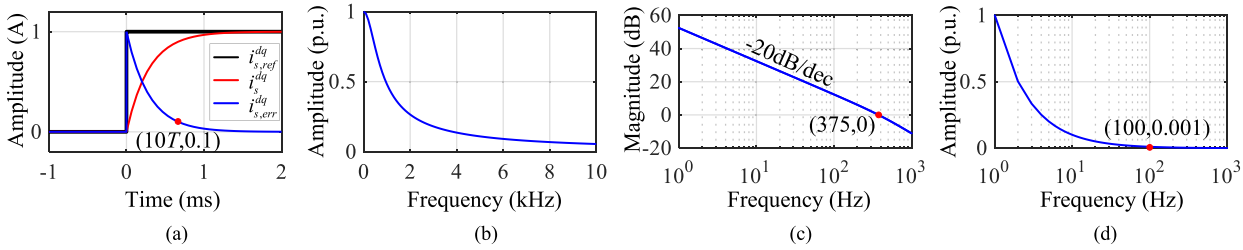

Fig. 15. Signals of the control system in the dq frame. (a) Signals in the closed-loop system. (b) Frequency spectrum of the open-loop input $i^{dq}_{s,\mathrm{err}}$. (c) Bode plot of the open-loop transfer function. (d) Frequency spectrum of the open-loop signal flow.

be obtained by

$$|I_{s,\mathrm{err}}(j\omega)| = \left| \int_{-\infty}^{\infty} e^{-at}\varepsilon(t)\cdot e^{-j\omega t}dt \right| = \frac{1}{\sqrt{a^2+\omega^2}} \tag{31}$$

as shown in Fig. 15(b). Obviously, the open-loop input signal is mainly in the low-frequency band.

Furthermore, the open-loop cutoff frequency f_c will be designed to be $f_s/40$, i.e., $f_c = 15000/40 = 375$ Hz. At the same time, in order to take into account the dynamic performance and robustness of the control system, the slope of the open-loop magnitude–frequency characteristic in low- and mid-frequency bands will be designed to be -20 dB/dec, as shown in Fig. 15(c).

Multiplying the waveforms in Fig. 15(b) and (c), the frequency spectrum of the open-loop transfer function signal flow can be obtained, as shown in Fig. 15(d). It indicates that, if the control system has been properly designed, the open-loop signal flow is mainly in the low-frequency band, specifically 0–100 Hz in this case. On this basis, it is a reasonable idea to consider only low-frequency bands when studying the dynamic decoupling of G^{dq}_{in2} and G^{dq}_{in3}.

B. LFETF-Based Dynamic Decoupling Controller for G^{dq}_{in2}

According to (24), the frequency characteristic of $G^{\alpha\beta}_{in2}$ is

$$G^{\alpha\beta}_{in2}(z)\Big|_{z=e^{j\omega T}} = e^{j\omega T}+1 \Rightarrow \begin{cases} \left|G^{\alpha\beta}_{\mathrm{in2}}\right| = 2\cos(\frac{\omega T}{2}) \\ \angle G^{\alpha\beta}_{in2} = \frac{\omega T}{2}. \end{cases} \tag{32}$$

When $f \in [0, 100\ \mathrm{Hz}]$, there is $\frac{\omega T}{2} = \frac{2\pi f T}{2} \in [0, 0.042\ \mathrm{rad}]$ ($T = 66.67\ \mu$s is the sampling period). Within this angle range, $\cos(\frac{\omega T}{2}) \approx 1$ obviously holds. Thus, the magnitude frequency characteristic of G^{dq}_{in2} in the low-frequency band is $|G^{\alpha\beta}_{in2}| \approx 2$, and the phase frequency characteristic is $\angle G^{\alpha\beta}_{in2} = \frac{\omega T}{2}$. Accordingly, $\angle G^{\alpha\beta}_{in2}$ in the low-frequency band can be equivalent to

$$\tilde{G}^{\alpha\beta}_{in2} = 2z^{\frac{1}{2}} \tag{33}$$

where the tilde at the top represents the LFETF. After dq transformation, it becomes

$$\tilde{G}^{dq}_{in2} = 2(ze^{j\omega_e T})^{\frac{1}{2}}. \tag{34}$$

Obviously, placing $\tilde{G}^{dq}_{in2}$ on the denominator of the decoupling controller can achieve cancellation, namely

$$G'_{dd2} = \frac{1}{\tilde{G}^{dq}_{in2}} = \frac{1}{2(ze^{j\omega_e T})^{\frac{1}{2}}}. \tag{35}$$

However, the fractional power of z cannot be realized in the actual control system, so the decoupling controller G'_{dd2} cannot be used directly. To solve this problem, set the numerator of the decoupling controller to $\tilde{G}^{\alpha\beta}_{in2}$, namely

$$G_{dd2} = \frac{\tilde{G}^{\alpha\beta}_{in2}}{\tilde{G}^{dq}_{in2}} = \frac{2z^{\frac{1}{2}}}{2(ze^{j\omega_e T})^{\frac{1}{2}}} = e^{-\frac{1}{2}j\omega_e T}. \tag{36}$$

The fractional powers of z are canceled, thereby ensuring the realizability of the decoupling controller.

According to (25), the complex transfer function G^{dq}_{in2} is written as

$$G^{dq}_{in2} = ze^{j\omega_e T}+1 = \underbrace{z\cos(\omega_e T)+1}_{G^{dq}_{in2,r}} + j\underbrace{z\sin(\omega_e T)}_{G^{dq}_{in2,i}}. \tag{37}$$

After adopting the proposed dynamic decoupling controller G_{dd2}, it becomes (without approximation)

$$\begin{aligned} G_{a2} &= G_{dd2}\cdot G^{dq}_{in2} = ze^{\frac{1}{2}j\omega_e T} + e^{-\frac{1}{2}j\omega_e T} \\ &= \underbrace{(z+1)\cos(\tfrac{1}{2}\omega_e T)}_{G_{a2,r}} + j\underbrace{(z-1)\sin(\tfrac{1}{2}\omega_e T)}_{G_{a2,i}}. \end{aligned} \tag{38}$$

To evaluate the dynamic decoupling performance, the magnitude ratio of the imaginary part ($|G_i|$) to the real part ($|G_r|$) is calculated based on (37) and (38), as shown in Fig. 16. The fundamental frequency is from 0 to 1500 Hz (1.5 times the rated fundamental frequency), and the signal frequency is from 0 to 100 Hz since the open-loop signal flow is mainly in the low-frequency band. It can be seen from Fig. 16(a) that the magnitude ratio of G^{dq}_{in2} increases as the fundamental frequency increases, which means an increase in cross coupling. The magnitude ratio after dynamic decoupling is shown in Fig. 16(b), which shows that the amplitude ratio is significantly reduced, that is, the cross coupling is alleviated. Comparing the A point in Fig. 16(a) and the C point in Fig. 16(b), the amplitude ratio of 0-Hz signal is reduced from 0.21 to 0 at the rated fundamental frequency 1000 Hz. Comparing the B point in Fig. 16(a) and the D point in Fig. 16(b), the amplitude ratio of 0-Hz signal is reduced from 0.33 to 0 at 1.5 times rated fundamental frequency 1500 Hz.

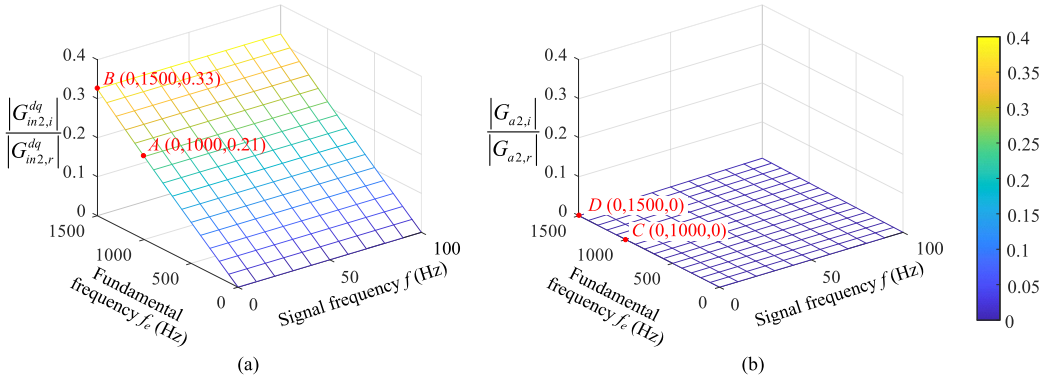

Fig. 16. Evaluation of the dynamic decoupling performance of G_{dd2} for G_{in2}^{dq}: the magnitude ratio of the imaginary part to the real part of the transfer function. (a) Original plant: G_{in2}^{dq}. (b) Plant after dynamic decoupling G_{a2}.

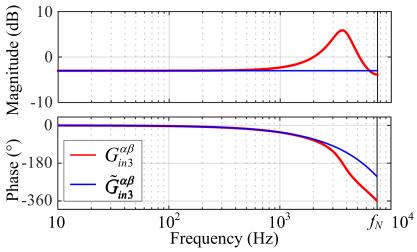

Fig. 17. Bode plot of $G_{in3}^{\alpha\beta}$ and $\tilde{G}_{in3}^{\alpha\beta}$.

Evidently, the dynamic decoupling of G_{in2}^{dq} is achieved through the LFETF-based decoupling controller G_{dd2}.

C. LFETF-Based Dynamic Decoupling Controller for G_{in3}^{dq}

According to (24), the frequency characteristic of $G_{in3}^{\alpha\beta}$ can be derived as

$$\left|G_{in3}^{\alpha\beta}(z)\right|_{z=e^{j\omega T}} \triangleq \frac{1}{A(\omega)} \angle G_{in3}^{\alpha\beta}(z)\Big|_{z=e^{j\omega T}} \triangleq -\varphi(\omega) \tag{39}$$

with

$$A(\omega) = \sigma^2 \sqrt{\begin{array}{l}(1+\frac{1}{\sigma^2})^2 - 4\frac{1}{\sigma}(1+\frac{1}{\sigma^2})\cos(\omega_r^* T)\cos(\omega T) \\ +\, 4\frac{1}{\sigma^2}[\cos^2(\omega_r^* T) + \cos^2(\omega T) - 1]\end{array}} \tag{40}$$

$$\begin{aligned}\varphi(\omega) = 2\omega T &+ \operatorname{actan}\left[\sin((\omega_r^* - \omega)T), \cos((\omega_r^* - \omega)T) - \tfrac{1}{\sigma}\right] \\ &+ \operatorname{actan}\left[-\sin((\omega_r^* + \omega)T), \cos((\omega_r^* + \omega)T) - \tfrac{1}{\sigma}\right]\end{aligned} \tag{41}$$

which is relatively complicated. Fortunately, it can be found from the Bode plot of $G_{in3}^{\alpha\beta}$ (red) in Fig. 17 that its amplitude is approximately constant, and its phase changes regularly in the low-frequency band. Therefore, (40) and (41) can be simplified as follows in the low-frequency band:

$$\begin{aligned}A(\omega) &\approx A(0) \\ &= \sigma^2 \sqrt{\left(1+\frac{1}{\sigma^2}\right)^2 - 4\frac{1}{\sigma}\left(1+\frac{1}{\sigma^2}\right)\cos(\omega_r^* T) + 4\frac{1}{\sigma^2}\cos^2(\omega_r^* T)}\end{aligned} \tag{42}$$

$$\varphi(\omega) \approx \rho\omega T. \tag{43}$$

ρ is obtained by fitting $\angle G_{in3}^{\alpha\beta}$ in the low-frequency band, which is calculated as

$$\rho = 0.3\sigma^2 - 1.7\sigma + 2.4. \tag{44}$$

Based on (39), (42), and (43), the LFETF of $G_{in3}^{\alpha\beta}$ is

$$\tilde{G}_{in3}^{\alpha\beta} = \frac{1}{A(0)} z^{-\rho}. \tag{45}$$

The Bode plot of $\tilde{G}_{in3}^{\alpha\beta}$ is shown in blue in Fig. 17, which confirms that $\tilde{G}_{in3}^{\alpha\beta}$ is equivalent to $G_{in3}^{\alpha\beta}$ in the low-frequency band.

After dq transformation, the LFETF becomes

$$\tilde{G}_{in3}^{dq} = \frac{1}{A(0)} (z e^{j\omega_e T})^{-\rho}. \tag{46}$$

Then, the decoupling controller is designed similarly to (36), namely

$$G_{dd3} = \frac{\tilde{G}_{in3}^{\alpha\beta}}{\tilde{G}_{in3}^{dq}} = \frac{\frac{1}{A(0)} z^{-\rho}}{\frac{1}{A(0)} (z e^{j\omega_e T})^{-\rho}} = e^{\rho j \omega_e T}. \tag{47}$$

According to (25), the complex transfer function G_{in3}^{dq} is written as

$$\begin{aligned}G_{in3}^{dq} &= \frac{1}{z^2 e^{2j\omega_e T} - 2\varepsilon\sigma z e^{j\omega_e T} + \sigma^2} \\ &= \underbrace{\frac{z^2\cos(2\omega_e T) - 2\varepsilon\sigma z\cos(\omega_e T) + \sigma^2}{M_{in3}}}_{G_{in3,r}^{dq}} \\ &\quad + j \underbrace{\frac{-z^2\sin(2\omega_e T) + 2\varepsilon\sigma z\sin(\omega_e T)}{M_{in3}}}_{G_{in3,i}^{dq}}\end{aligned} \tag{48}$$

with

$$\begin{aligned}M_{in3} = &\left(z^2\cos(2\omega_e T) - 2\varepsilon\sigma z\cos(\omega_e T) + \sigma^2\right)^2 \\ &+ \left(z^2\sin(2\omega_e T) - 2\varepsilon\sigma z\sin(\omega_e T)\right)^2\end{aligned} \tag{49}$$

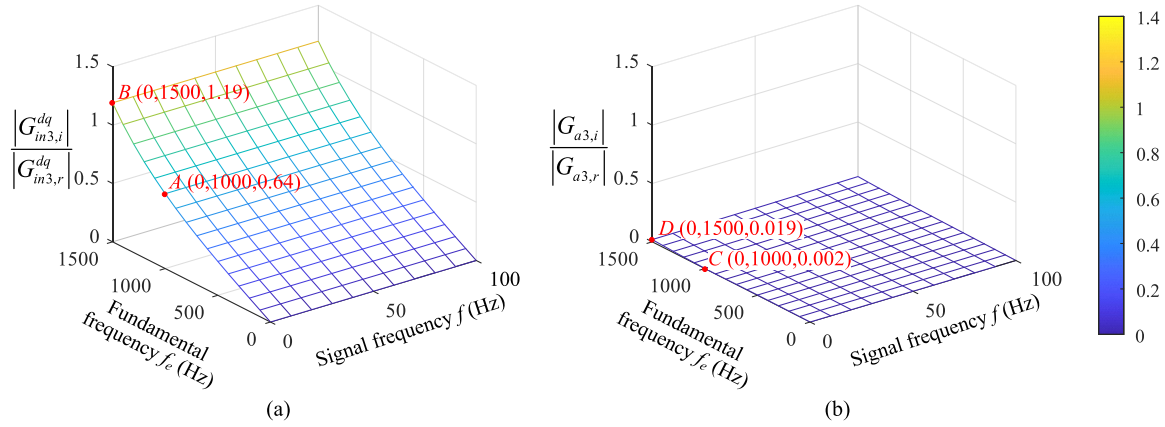

Fig. 18. Evaluation of the dynamic decoupling performance of G_{dd3} for G_{in3}^{dq}: The magnitude ratio of the real part to the imaginary part of the transfer function. (a) Original plant: G_{in3}^{dq}. (b) Plant after dynamic decoupling: G_{a3}.

where $\varepsilon = \cos(\omega_r^* T)$. After adopting the proposed dynamic decoupling controller G_{dd3}, it becomes (without approximation)

$$G_{a3} = G_{dd3} \cdot G_{in3}^{dq}$$
$$= \frac{1}{z^2 e^{(2-\rho)j\omega_e T} - 2\varepsilon\sigma z e^{(1-\rho)j\omega_e T} + \sigma^2 e^{-\rho j\omega_e T}}$$
$$= \underbrace{\frac{z^2\cos((2-\rho)\omega_e T) - 2\varepsilon\sigma z\cos((1-\rho)\omega_e T) + \sigma^2\cos(\rho\omega_e T)}{M_{a3}}}_{G_{a3,r}}$$
$$+ j\underbrace{\frac{-z^2\sin((2-\rho)\omega_e T) + 2\varepsilon\sigma z\sin((1-\rho)\omega_e T) + \sigma^2\sin(\rho\omega_e T)}{M_{a3}}}_{G_{a3,i}} \tag{50}$$

with

$$M_{a3} =$$
$$\left[z^2\cos((2-\rho)\omega_e T) - 2\varepsilon\sigma z\cos((1-\rho)\omega_e T) + \sigma^2\cos(\rho\omega_e T)\right]^2$$
$$+ \left[z^2\sin((2-\rho)\omega_e T) - 2\varepsilon\sigma z\sin((1-\rho)\omega_e T) - \sigma^2\sin(\rho\omega_e T)\right]^2 \tag{51}$$

Based on (48)–(51), the magnitude ratio of the imaginary part to the real part is shown in Fig. 18. It can be seen from Fig. 18(a) that the magnitude ratio of G_{in3}^{dq} increases significantly as the fundamental frequency increases, which means the aggravation of cross coupling. In particular, the A point in Fig. 18(a) shows that the amplitude ratio of 0-Hz signal is up to 0.64 at the fundamental frequency 1000 Hz, which means that the cross coupling is serious. After dynamic decoupling, this amplitude ratio is significantly reduced to 0.002, as shown by the C point in Fig. 18(b). In addition, comparing the B point in Fig. 18(a) and the D point in Fig. 18(b), the amplitude ratio of 0-Hz signal is reduced from 1.19 to 0.019 at 1.5 times rated fundamental frequency 1500 Hz. Evidently, the dynamic decoupling effect of G_{dd3} for G_{in3}^{dq} is verified.

D. Overall Dynamic Decoupling Controller

According to (26), (36), and (47), the overall dynamic decoupling controller is

$$G_{dd}(z) = G_{dd1}G_{dd2}G_{dd3} = \frac{ze^{j\omega_e T} - p}{z - p_1} \cdot e^{(-\frac{1}{2}+\rho)j\omega_e T} \tag{52}$$

which combines the existing direct cancellation method (G_{dd1}) and the proposed LFETF-based method (G_{dd2}, G_{dd3}).

V. Open-Loop Bode Plot Design and Robustness Evaluation

Fig. 19 shows the overall control diagram of the proposed current control method for the CSI-fed HSPMSM drive, where the black boxes represent the original plant, the red boxes represent the inner-loop MSFAD part, and the blue boxes represent the outer-loop current control part.

A. Design of the Open-Loop Transfer Function Bode Plot

According to (25) and (52), the dq frame transfer function after MSFAD and dynamic decoupling is

$$G_a = G_{dd}G_{in}^{dq}$$
$$= e^{(-\frac{1}{2}+\rho)j\omega_e T}\frac{\eta(ze^{j\omega_e T}+1)}{(z-p_1)(ze^{j\omega_e T} - \sigma e^{j\omega_r^* T})(ze^{j\omega_e T} - \sigma e^{-j\omega_r^* T})}. \tag{53}$$

On this basis, a PI controller is adopted to adjust the amplitude and phase of the open-loop transfer function, as shown in Fig. 19. Also, the integrator in the PI controller ensures the zero steady-state error tracking of the motor current reference at the

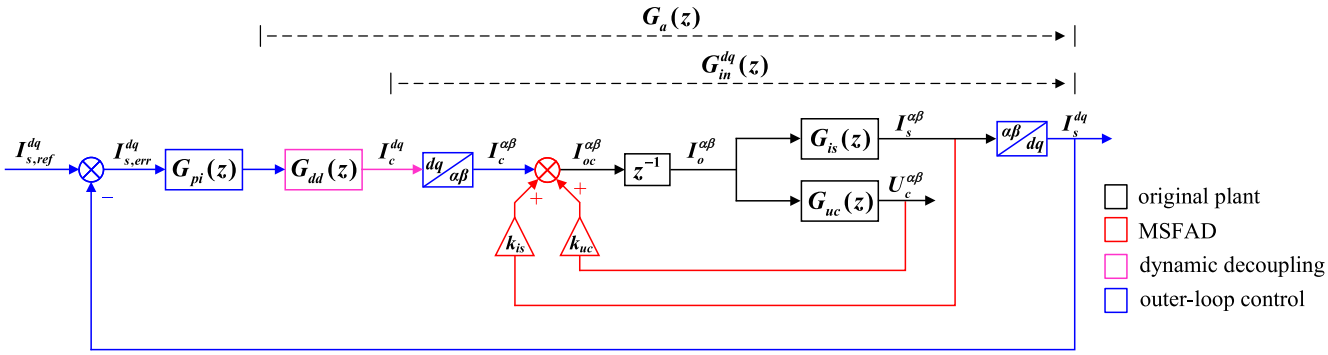

Fig. 19. Overall control diagram of the proposed control method for the CSI-fed HSPMSM drive.

fundamental frequency. The PI controller is expressed as

$$G_{\rm pi} = k\frac{z-\delta}{z-1}. \tag{54}$$

Thus, the open-loop transfer function is

$$\begin{aligned} G_{\rm ol} &= G_{\rm pi}G_a \\ &= \frac{e^{(-\frac{1}{2}+\rho)j\omega_e T}\cdot k\eta(z-\delta)(ze^{j\omega_e T}+1)}{(z-1)(z-p_1)(ze^{j\omega_e T}-\sigma e^{j\omega_r^* T})(ze^{j\omega_e T}-\sigma e^{-j\omega_r^* T})}. \end{aligned} \tag{55}$$

Note that the frequency characteristics of the first-order term in the z domain are

$$\begin{aligned} &G_1(z) = z - c \\ &\Rightarrow \begin{cases} |G_1(z)|_{z=e^{j\omega T}} = \sqrt{(\cos(\omega T)-a)^2+\sin^2(\omega T)} \triangleq A_1(\omega,c) \\ \angle G_1(z)|_{z=e^{j\omega T}} = \operatorname{actan}\left(\frac{\sin(\omega T)}{\cos(\omega T)-c}\right) \triangleq \varphi_1(\omega,c). \end{cases} \end{aligned} \tag{56}$$

It can be deduced by (56) that

$$G_1' = z+1 \Rightarrow |G'_1| = 2\cos\left(\frac{\omega T}{2}\right), \angle G_1' = \frac{\omega T}{2} \tag{57}$$

$$G_1'' = z-1 \Rightarrow |G_1''| = 2\sin\left(\frac{\omega T}{2}\right), \angle G_1'' = \frac{\pi}{2}+\frac{\omega T}{2}. \tag{58}$$

Also, it should be noted that the frequency characteristic will shift to the left after the dq transformation, namely

$$G^{dq}(z) = G^{\alpha\beta}(ze^{j\omega_e T}) \Rightarrow \begin{cases} |G^{\rm dq}|(\omega) = |G^{\alpha\beta}|(\omega+\omega_{\rm e}) \\ \angle G^{dq}(\omega) = \angle G^{\alpha\beta}(\omega+\omega_e). \end{cases} \tag{59}$$

According to (39), (40), (43), and (56)–(59), the frequency characteristics of the open-loop transfer function are

$$|G_{\rm ol}(z)|_{z=e^{j\omega T}} = \frac{k\eta\cos\left(\frac{(\omega+\omega_e)T}{2}\right)A_1(\omega,\delta)}{\sin\left(\frac{\omega T}{2}\right)A(\omega+\omega_e)A_1(\omega,p_1)} \tag{60}$$

$$\angle G_{\rm ol}(z)|_{z=e^{j\omega T}} = -\frac{\pi}{2} - \rho\omega T + \varphi_1(\omega,\delta) - \varphi_1(\omega,p_1). \tag{61}$$

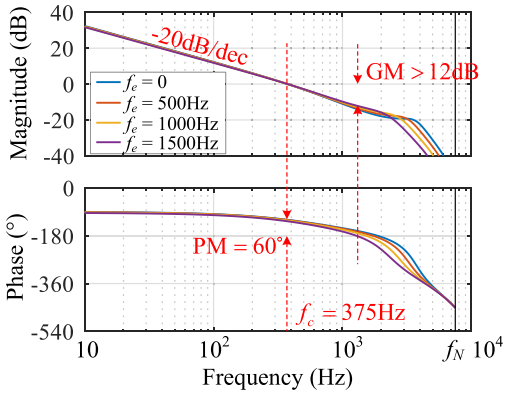

Fig. 20. Bode plot of the open-loop transfer function.

The desired cutoff frequency of $G_{\rm ol}$ is set to $f_c = f_s/40 = 375$ Hz, and there is $\omega_c = 2\pi f_c$. The desired phase margin is set to PM $= 60^\circ = \pi/3$ rad. Thus, substituting ω_c into (61) gives

$$\begin{aligned} \angle G_{\rm ol}(\omega_c) &= -\frac{\pi}{2} - \lambda\omega_c T + \varphi_1(\omega_c,\delta) - \varphi_1(\omega_c,p_1) \\ &= {\rm PM} - \pi. \end{aligned} \tag{62}$$

Based on (56) and (62), the zero of the PI controller can be derived as

$$\delta = \cos(\omega_c T) - \frac{\sin(\omega_c T)}{\tan\left({\rm PM} - \frac{\pi}{2} + \rho\omega_c T + \varphi_1(\omega_c,p_1)\right)}. \tag{63}$$

Furthermore, substituting ω_c into (60) gives

$$|G_{\rm ol}|(\omega_c) = \frac{k\eta\cos\left(\frac{(\omega_c+\omega_e)T}{2}\right)A_1(\omega_c,\delta)}{\sin\left(\frac{\omega_c T}{2}\right)A(\omega_c+\omega_e)A_1(\omega_c,p_1)} = 1. \tag{64}$$

Then, the PI gain can be derived from (64) as

$$k = \frac{\sin\left(\frac{\omega_c T}{2}\right)A(\omega_c+\omega_e)A_1(\omega_c,p_1)}{\eta\cos\left(\frac{(\omega_c+\omega_e)T}{2}\right)A_1(\omega_c,\delta)}. \tag{65}$$

With the above design process, the Bode plot of the open-loop transfer function $G_{\rm ol}(z)$ is shown in Fig. 20, and the system parameters are listed in Table I. It can be seen that, as the fundamental frequency f_e increases from 0 to 1500 Hz, the

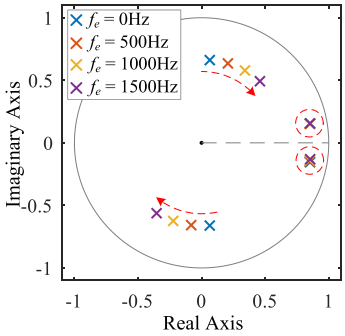

Fig. 21. Pole of the closed-loop transfer function when the fundamental frequency f_e changes.

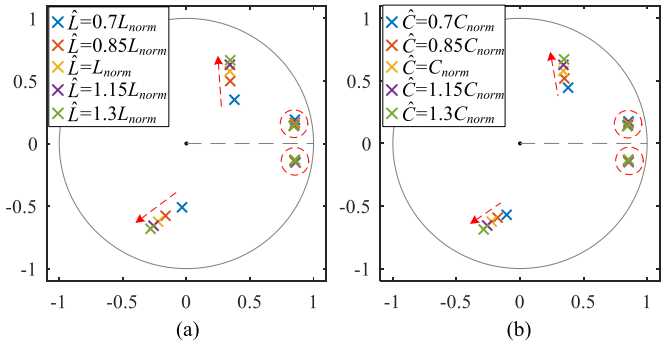

Fig. 22. Pole of the closed-loop transfer function when the estimated parameters $\hat{L}$ and $\hat{C}$ change ($f_e = 1000$ Hz). (a) $\hat{L}$ from $0.7L_{\text{norm}}$ to $1.3L_{\text{norm}}$. (b) $\hat{C}$ from $0.7C_{\text{norm}}$ to $1.3C_{\text{norm}}$.

cutoff frequency f_c is kept at 375 Hz, and the PM is kept at 60°. Also, since the resonance frequency is increased and the resonance peak is suppressed through the MSFAD, the GM is greater than 12 dB, which is large enough. In addition, it is obvious that the slope of G_{ol} in the low- and mid-frequency bands is about −20 dB/dec, which means that the control system has good dynamic performance and robustness. Since the open-loop Bode plot already meets the design requirements, there is no need to introduce other compensators in the control system.

B. Robustness Evaluation

To evaluate the robustness of the proposed control method, the closed-loop pole diagram of the control system is drawn with the motor resistance R considered in the system model. Fig. 21 shows the closed-loop pole when the fundamental frequency f_e changes (noncritical poles are omitted). From the part circled in red, it can be seen that the dominant pole of the system hardly changes with the fundamental frequency, which shows that the proposed method can maintain consistent dynamic performance when the fundamental frequency changes. At the same time, it can be seen from the red dotted arrow that the other pair of poles moves clockwise as the fundamental frequency rises and has no tendency to move outside the unit circle. This shows that the proposed control method can maintain system stability when the fundamental frequency changes in a wide range.

Fig. 22 shows the closed-loop poles when the estimated parameters $\hat{L}$ and $\hat{C}$ change. $\hat{L}$ and $\hat{C}$ are used to calculate the controller parameters, the model parameters R, L, and C are set to normal values as listed in Table I, and $f_e = 1000$ Hz. As shown in Fig. 22(a), the position of the dominant pole circled in red almost remains unchanged when $\hat{L}$ changes from $0.7L_{\text{norm}}$ to $1.3L_{\text{norm}}$ (the subscript $_{\text{norm}}$ represents the normal value listed in Table I). The other pole pair has a tendency to move outside the unit circle, as shown by the red dotted line, but the poles are still within the unit circle. Fig. 22(b) shows the closed-loop poles when $\hat{C}$ changes from $0.7C_{\text{norm}}$ to $1.3C_{\text{norm}}$, which indicates that the change of the pole is similar to Fig. 22(a). This is because the positions of L and C in the system model are similar, as shown in (4) and (5). It is obvious from Fig. 22 that, under the ±30% error of $\hat{L}$ and $\hat{C}$, closed-loop poles remain within the unit circle, and there is still a certain distance from the boundary of the unit circle, which verifies the parameter robustness of the proposed control method.

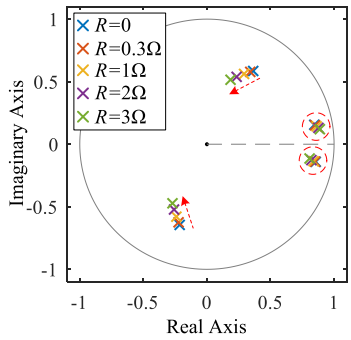

Fig. 23. Pole of the closed-loop transfer function when motor resistance R changes ($f_e = 1000$ Hz).

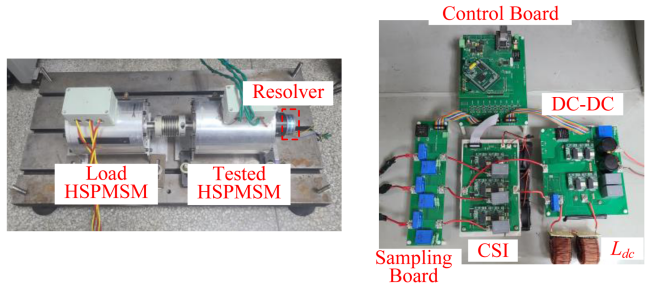

Fig. 24. Experimental platform of the tested CSI-fed HSPMSM drive.

On the other hand, Fig. 23 shows the closed-loop poles when motor resistance R changes from 0 to 3 Ω ($10R_{\text{norm}}$). The changing R is adopted in the system model, the other parameters are set to normal values, and $f_e = 1000$ Hz. It can be seen that as R increases, the position of the dominant pole circled in red almost remains unchanged, while the other pair of poles tends to move toward the center of the circle. This indicates that the motor resistance is beneficial to the stability of the control system and also proves the feasibility of adopting the model that ignores resistance for control design in the CSI-fed system, as described in Section II-A.

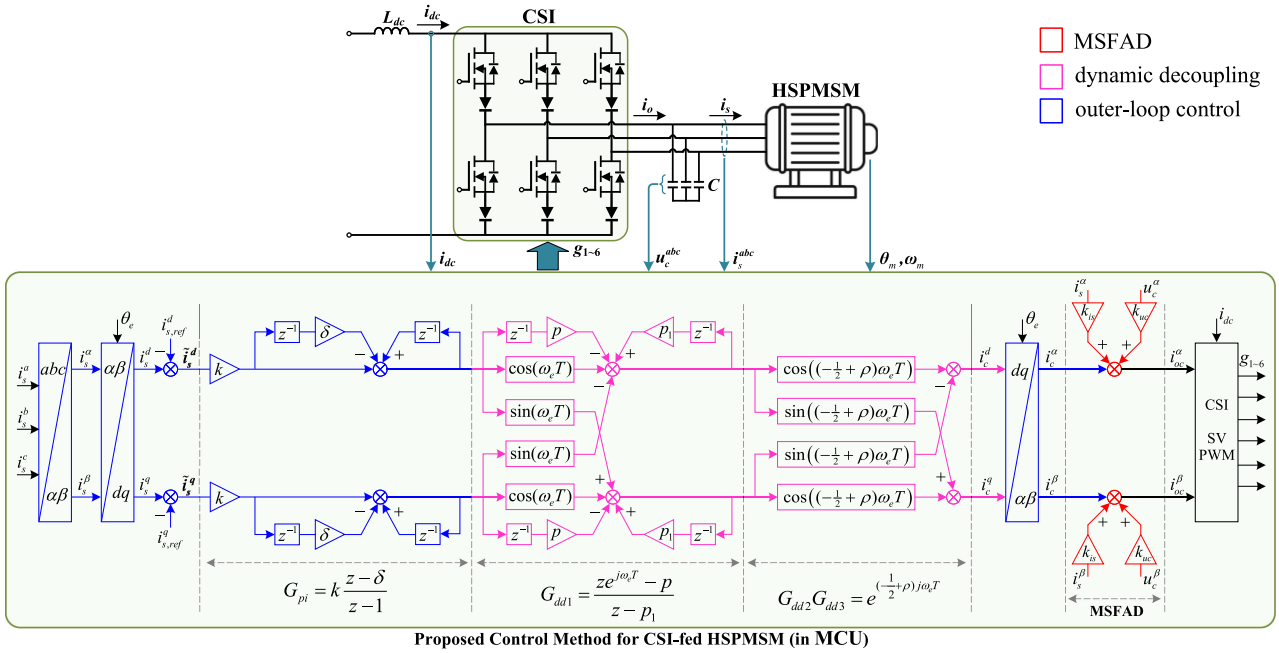

Fig. 25. Diagram of the control system and the digital implementation of the proposed control method for the CSI-fed HSPMSM.

TABLE II
PARAMETERS OF THE PROPOSED CONTROL METHOD (CALCULATED IN SEQUENCE)

Symbol	Parameter	Calculation Equation and the Used Parameters	Value
ω_r	Natural resonance frequency	Eq(3) with L, C	$2814\times2\pi$ rad
η	Coefficient of the system transfer function $G_{is}(z)$ in (4)	Eq(6) with ω_r, T	0.618
μ	Coefficient of the system transfer function $G_{uc}(z)$ in (5)	Eq(6) with L, C, T, ω_r	6.536
ω_r^*	Desired resonance frequency in MSFAD	Eq(20) with ω_r	$3564\times2\pi$ rad
σ	Desired modulus of the resonance poles in MSFAD	Preset in Eq(20)	0.7
k_{uc}	Voltage feedback coefficient of MSFAD	Eq(15) with $T, \omega_r, \mu, \omega_r^*, \sigma$	0.0090
k_{is}	Current feedback coefficient of MSFAD	Eq(16) with $T, \omega_r, \eta, \omega_r^*, \sigma$	0.62
p	Real pole of the plant after MSFAD $G_{in}^{\alpha\beta}(z)$ in (21)	Eq(17) with $T, \omega_r, \omega_r^*, \sigma$	0.66
p_1	Pole of the decoupling controller G_{dd1} in (26)	Preset	0.75
ρ	Exponential coefficient of the decoupling controller G_{dd3} in (47)	Eq(44) with σ	1.36
ω_c	Cutoff frequency of the open-loop transfer function	Preset	$375\times2\pi$ rad
PM	Phase margin of the open-loop transfer function	Preset	60°
δ	Zero of the PI controller G_{pi} in (54)	Eq(63) with T, p_1, ρ, ω_c, PM	0.43
k	Gain of the PI controller G_{pi} in (54)	Eq(65) with $T, \omega_e, \eta, p_1, \omega_c$, PM, δ	0.076

Basic parameters are motor inductance L, filter capacitor C, sampling period T, and motor fundamental frequency ω_e.
Red symbols represent the parameters that need to be used in the implementation of the proposed control method, as shown in Fig. 25.
In the calculation of k, ω_e is set to the rated fundamental frequency, namely, $\omega_e = 1000 \times 2\pi$ rad.

VI. EXPERIMENTAL VERIFICATION

Fig. 25 shows the diagram of the control system and the digital implementation of the proposed control method for the CSI-fed HSPMSM. The experimental platform of the CSI-fed HSPMSM drive is shown in Fig. 24, in which a front-stage dc–dc converter is used to maintain dc current of the CSI. The tested HSPMSM is coaxially connected to a similar HSPMSM with three-phase load resistors. Under the rated speed 12 000 r/min, the load current i_q is about 5 A and the system power is about 1.3 kW.

A resolver model TS2640N321E64 supplied by Tamagawa is installed on the tested HSPMSM to measure the rotor position and speed, and the resolver-to-digital converter uses AD2S1210 supplied by Analog Devices. The adopted MCU is TI TMS320F28377D with the 200-MHz system clock, and the experimental data are sent to the host computer by the Ethernet module. The system parameters are listed in Table I. The parameters of the proposed control method and their calculation method are summarized in Table II. Note that the parameters listed in Table II should be calculated in sequence, and each parameter is composed of the basic parameters (L, C, T, ω_e) and the parameters that have already been calculated.

In this study, the target application is the high-speed ($n >$ 10 000 r/min) and high-power (hundreds of kilowatts) PMSM drive. Usually, the ratio of switching frequency to fundamental frequency is required to be higher than 8 in the high-speed

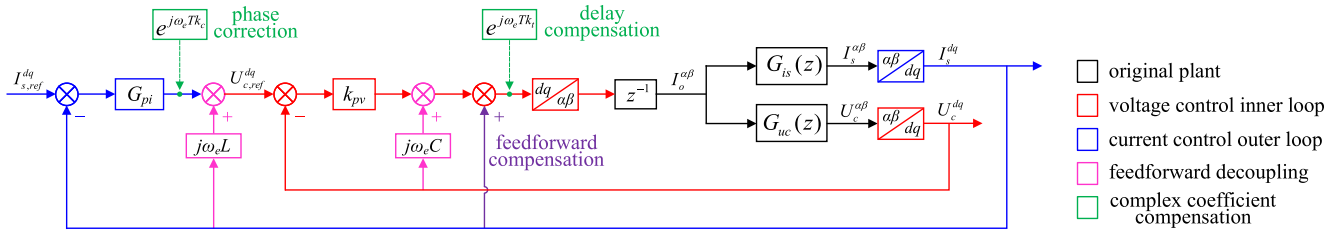

Fig. 26. Control diagram of the existing methods based on voltage feedback AD [9], [10].

PMSM drive to ensure the feasibility of filter design, acceptable motor current steady-state performance (THD), and dynamic performance (step response time). The fundamental frequency of the tested HSPMSM is 1 kHz, so the switching frequency should be higher than 8 kHz and is selected to 10 kHz in this experimental platform. As well known, the diode is used in series with ordinary switching devices (MOSFET or insulated gate bipolar transistor) to obtain reverse voltage blocking capability in the CSI. In this case, it is difficult for Si-based devices to achieve the 10-kHz switching frequency due to the large power loss. Therefore, the SiC-based devices (SiC-based MOSFET and Schottky diode) are necessary to reduce the power loss, thus achieving a switching frequency of around 10 kHz. At present, the single SiC-based device cannot reach the power level of hundreds of kilowatts, so multiple SiC-based devices need to be connected in parallel or commercial high-power SiC modules need to be used. On the other hand, there are currently new monolithic switching devices with reverse voltage blocking capability, which mainly include the GaN-based dual-gate monolithic bidirectional switch [29] and the SiC-based monolithic reverse blocking transistor [30]. These new monolithic switching devices can eliminate series diodes, thus further reducing power losses.

A. Comparison With the Existing Methods Based on Voltage Feedback AD

To illustrate the improvements of the proposed MSFAD-based control method for the CSI-fed HSPMSM, this article experiments with the two existing control methods [9], [10], which adopt capacitor voltage feedback AD and are designed for the conventional CSI-fed PMSM with low carrier ratios. The control diagram of these two existing methods is shown in Fig. 26. It can be seen that the voltage control inner loop is adopted, which can be regarded as the voltage feedback AD. The traditional feedforward decoupling method is implemented, as marked by magenta. In [10], the complex coefficient compensations are proposed to further improve the dynamic decoupling performance at low carrier ratios, as marked by green.

The P-type voltage controllers and PI-type current controllers of the two existing methods are

$$k_{pv} = 2\pi f_1 C, \quad G_{\mathrm{pi}} = \frac{(k_{pi} + k_{pii}T)z - k_{pi}}{z - 1} \tag{66}$$

with $k_{pi} = 2\pi f_2 L$ and $k_{ii} = 2\pi f_2 R$. With the parameters of the tested CSI-fed HSPMSM system, f_1 and f_2 are tuned to 1000 and 1200 Hz, respectively. The complex coefficient compensation items for these two methods are set as follows.

Existing Method 1 [9]: $k_t = 1$ and $k_c = 0$, which mean that only basic digital delay compensation is used.

Existing Method 2 [10]: $k_t = 1.5$ and $k_c = 1$, which are tuned according to the design principle in [10].

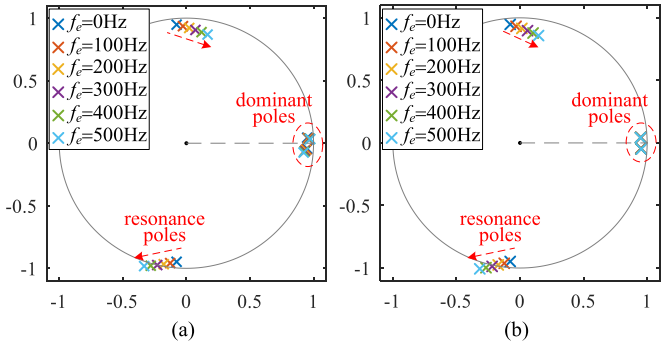

Fig. 27. Closed-loop poles of the existing methods based on voltage feedback AD, the fundamental frequency f_e from 0 to 500 Hz. (a) Existing Method 1 [9]. (b) Existing Method 2 [10].

The closed-loop poles of the tested CSI-fed HSPMSM system when adopting the existing methods are shown in Fig. 27; the fundamental frequency f_e is set to 0–500 Hz (0–6000 r/min). It can be seen from Fig. 27(a) that, when adopting *Existing Method 1*, the resonance pole drifts out of the unit circle at 300 Hz, which means that the control system becomes unstable. It is shown in Fig. 27(b) that the stable boundary frequency is also 300 Hz when adopting *Existing Method 2*, which is because the complex compensation terms are designed for dynamic decoupling and do not enhance the stability range. In contrast, proposed method can remain stable from 0 to 1500 Hz, as shown in Fig. 21.

Fig. 28 shows the comparison of acceleration performance with the existing methods. Fig. 28(a) and (b) indicates that the control system adopting existing methods loses stability when accelerating to close to 4500 r/min (375 Hz), which is still far from the rated speed of 12 000 r/min (1000 Hz). It is observed that the stable frequency range in the experiments (0–375 Hz) is larger than that in the closed-loop pole diagram of Fig. 27 (0–300 Hz). This is because there are other resistances in addition to the motor resistance, including the resistances of wires, filter capacitors, and semiconductor devices. These unmodeled resistances are intrinsic damping in the system and will extend the stability range. In comparison, Fig. 28(c) shows

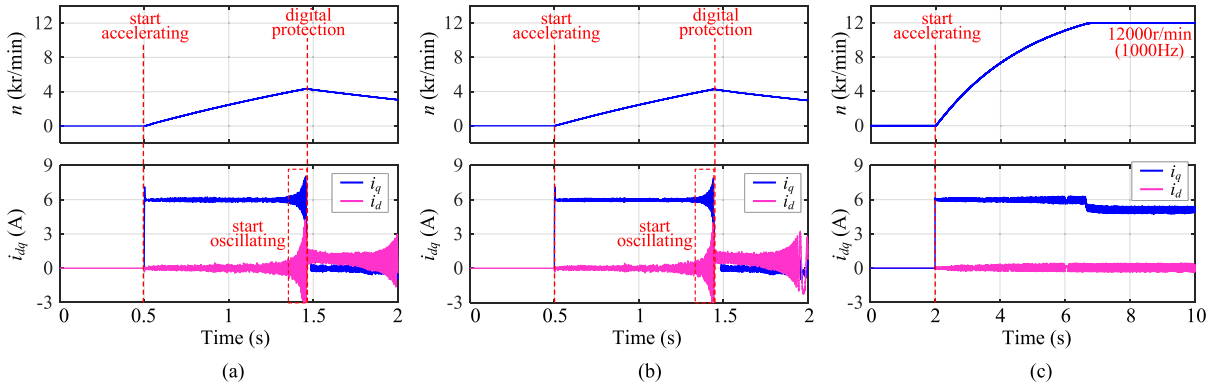

Fig. 28. Experimental results: Acceleration performance comparison with the existing methods based on voltage feedback AD. (a) Existing method 1. (b) Existing method 2. (c) Proposed method.

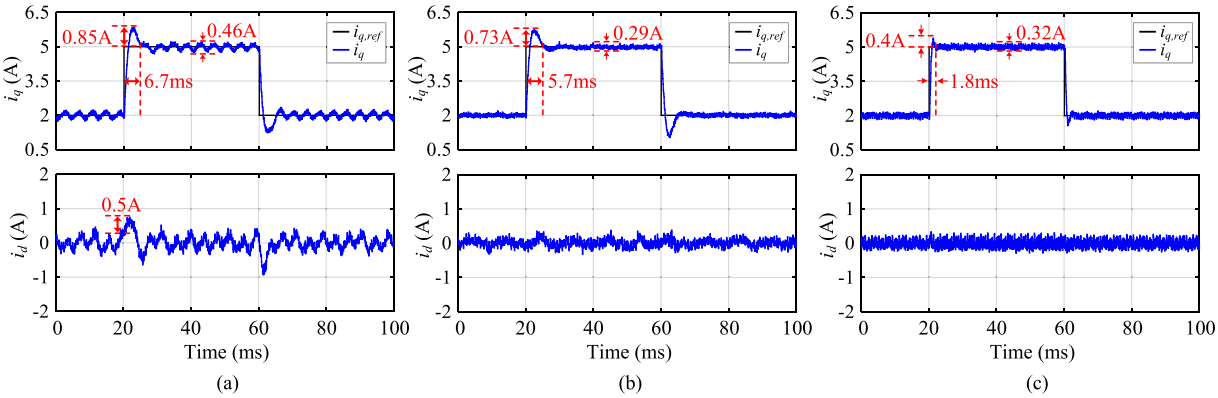

Fig. 29. Experimental results: Dynamic performance comparison with the existing methods based on voltage feedback AD, $n = 3000$ r/min (250 Hz). (a) Existing method 1. (b) Existing method 2. (c) Proposed method.

that the HSPMSM can accelerate to the rated speed 12 000 r/min stably when adopting the proposed method.

The comparisons of dynamic performance at 3000 r/min (250 Hz) are shown in Fig. 29, in which i_q steps from 2 to 5 A at 20 ms and returns to 2 A at 60 ms, and i_d reference is set to 0. Comparing the experimental results of *Existing Method 1* [see Fig. 29(a)], *Existing Method 2* [see Fig. 29(b)], and the proposed method [see Fig. 29(c)], it can be seen that the settling times of step response are 6.7, 5.7, and 1.8 ms, respectively, and the overshoots are 0.85 A (28.3%), 0.73 A (24.3%), and 0.4 A (13.3%), respectively, which mean that the dynamic performance of the proposed method is improved. In addition, during the 3-A step response of i_q at 20 ms, the fluctuation of i_d are 0.5 A (16.7%) when adopting *Existing Method 1*. By contrast, there is almost no fluctuation in i_d when adopting *Existing Method 2* and the proposed method, which indicates that the complex compensation items in [10] and the decoupling controller proposed in this article both have dynamic decoupling effects. On the other hand, it can be seen that the i_q steady-state fluctuation of *Existing Method 1* is 0.46 A, which is larger than those of *Existing Method 2* (0.29 A) and the proposed method (0.32 A).

In summary, *Existing Method 2* has better decoupling performance and steady-state performance than *Existing Method 1*. Compared with *Existing Method 2*, the proposed method further significantly improves dynamic performance. More importantly, the proposed method can stably accelerate the HSPMSM to the rated speed 12 000 r/min, but these existing methods can only stably accelerate to about 4500 r/min. It is found that a larger frequency stability range can be obtained by adjusting f_1 and f_2 in these existing methods, but at the same time, the dominant poles will be too close to the unit circle boundary, resulting in unacceptable dynamic performance. The above comparisons indicate that the MSFAD is more stable than voltage feedback AD in the CSI-fed HSPMSM system and also verify the effectiveness of the proposed control method.

B. *dq*-Axis Decoupling Performance

To evaluate the performance of the proposed LFETF-based decoupling method, three cases are set up for experimental comparisons, which are specific as follows.

Case 1: The decoupling controller $G_{dd} = 1$, which means no decoupling measures are taken.

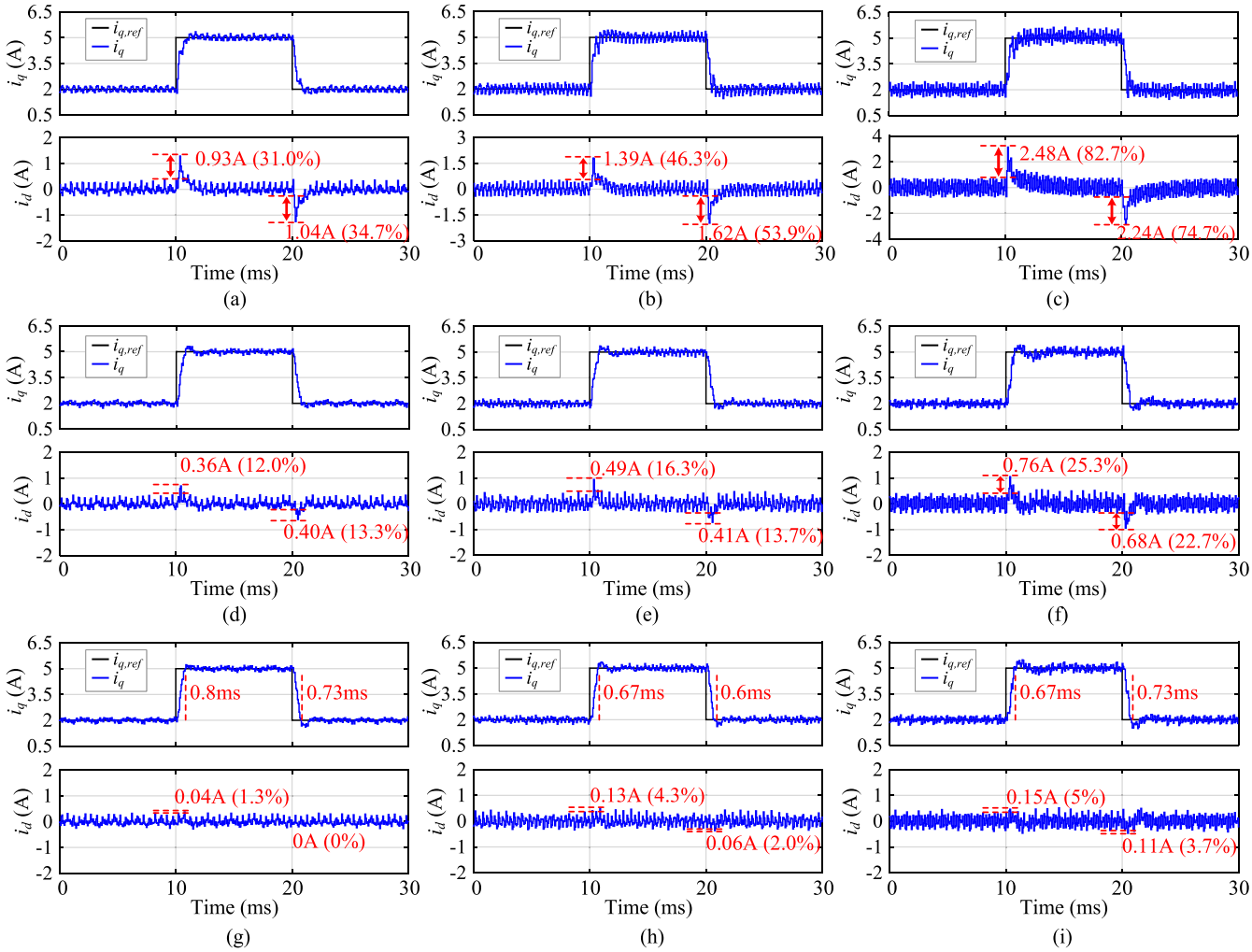

Fig. 30. Experimental results for decoupling performance evaluation: the q-axis current step responses of Cases 1–3 at 6000, 9000, and 12 000 r/min. (a) Case 1: $n = 6000$ r/min. (b) Case 1: $n = 9000$ r/min. (c) Case 1: $n = 12\,000$ r/min. (d) Case 2: $n = 6000$ r/min. (e) Case 2: $n = 9000$ r/min. (f) Case 2: $n = 12\,000$ r/min. (g) Case 3: $n = 6000$ r/min. (h) Case 3: $n = 9000$ r/min. (i) Case 3: $n = 12\,000$ r/min.

Case 2: $G_{dd} = G_{dd1}$, which means only using the existing direct cancellation method.

Case 3: $G_{dd} = G_{dd1}G_{dd2}G_{dd3}$, which means using both the existing direct cancellation method G_{dd1} and the proposed LFETF-based decoupling method G_{dd2}, G_{dd3}.

The experimental comparisons of Cases 1–3 at the speed of 6000, 9000, and 12 000 r/min are shown in Fig. 30, in which i_q steps from 2 to 5 A at 10 ms and returns to 2 A at 20 ms, and i_d reference is set to 0. The fluctuations of i_d during the step response of i_q are marked in Fig. 30, by which the dq-axis coupling degree can be evaluated. The i_d fluctuations during the +3 A step response of i_q are summarized in Fig. 31. It can be seen that, in Case 1, i_d fluctuations are 0.93 A (31.0%) at 6000 r/min, 1.39 A (46.3%) at 9000 r/min, and 2.48 A (82.7%) at 12 000 r/min. Obviously, the dq-axis coupling becomes more and more serious as the speed increases when no decoupling measures are taken (Case 1). It is also shown in Fig. 31 that the i_d fluctuations of Case 2 are mitigated compared with that of Case 1, but the i_d fluctuation at the rated speed 12 000 r/min

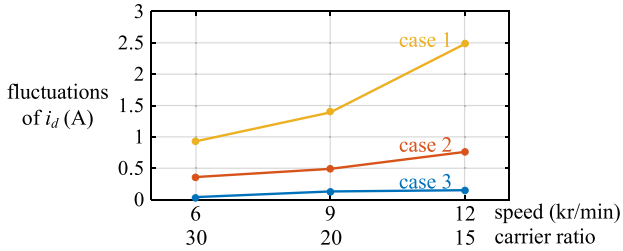

Fig. 31. Comparison of the dq-axis coupling degree in Fig. 30: the d-axis current fluctuations during the q-axis current step response of Cases 1–3 at 6000, 9000, and 12 000 r/min.

is 0.76 A (25.3%), which is still relatively large. This indicates that the existing direct cancellation method can only partially solve the dq-axis coupling problem. In contrast, the i_d fluctuations of Case 3 are reduced to 0.15 A (5%) at 12 000 r/min, which is significantly improved compared to Cases 1 and 2, and is already small enough. These experimental comparisons

TABLE III
RISE (OR FALL) TIME OF THE q-AXIS CURRENT STEP RESPONSES

Speed	Rise Time (at $t = 10$ ms)	Fall Time (at $t = 20$ ms)
6000 r/min	0.8 ms (12 T)	0.73 ms (11 T)
9000 r/min	0.67 ms (10 T)	0.6 ms (9 T)
12 000 r/min	0.67 ms (10 T)	0.73 ms (11 T)

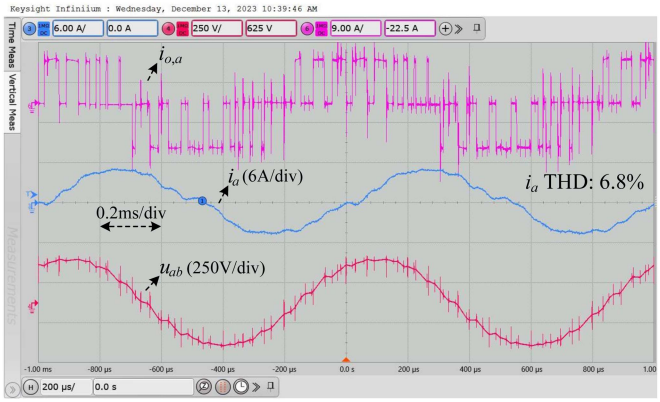

Fig. 32. Experimental results of steady-state performance at 12 000 r/min (1000 Hz): CSI output current $i_{o,a}$, HSPMSM phase current i_a, and line voltage u_{ab}.

prove the effectiveness of the proposed LFETF-based dynamic decoupling method.

C. Dynamic Performance

The step response times of the proposed method are marked in Fig. 30(g)–(i) and summarized in Table III, which are in the range of 0.6–0.8 ms (9–12 T) at the speeds of 6000, 9000, and 12 000 r/min. This indicates that the proposed current control method has a relatively fast dynamic performance, and the dynamic performance remains consistent at different speeds, which confirms the theoretical analysis of Fig. 21 that the dominant pole remains unchanged when the fundamental frequency changes.

D. Steady-State Performance

The experimental results of CSI output current $i_{o,a}$, HSPMSM phase current i_a, and line voltage u_{ab} after accelerating to 12 000 r/min are shown in Fig. 32. It can be seen that the line voltage is close to sinusoidal, which is significantly better than the pulse voltage in the VSI-fed system. Benefiting from the sinusoidal terminal voltage, the current THD (6.8%) is in a relatively small range from the perspective of HSPMSM applications. Increasing the filter capacitance can decrease the natural resonance frequency f_r and improve the high-frequency filtering ability, thus further reducing the THD. However, it should be noted that larger capacitance will increase system size and cost and reduce efficiency.

Also, it is obvious from the waveform of $i_{o,a}$ that CSI only outputs a limited number of pulses in one fundamental period,

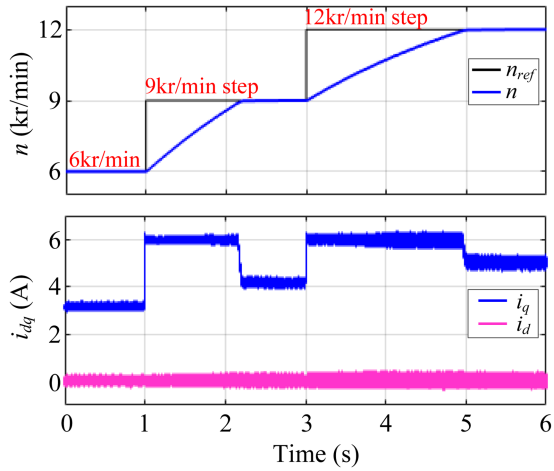

Fig. 33. Experimental results under speed step response: HSPMSM speed n and its reference n_{ref}, d-axis current i_d, and q-axis current i_q.

which reflects that the system is in the low-carrier-ratio condition. It should be noted that the CSI not only outputs the active current supplied to the motor in the q-axis direction but also outputs a certain reactive current supplied to the filter capacitor in the d-axis direction. Therefore, the CSI out current $i_{o,a}$ and motor phase current i_a have a certain phase difference.

E. Control Performance Under Speed Step Response

Fig. 33 shows the experimental results of HSPMSM speed n and its reference n_{ref}, d-axis current i_d, and q-axis current i_q under speed step response. The n_{ref} steps from 6000 to 9000 r/min at $t = 1$ s, and further steps to 12 000 r/min at $t = 3$ s. The experimental results indicate that the proposed control method (including the MSFAD-based resonant controller, the dynamic decoupling controller G_{dd}, and the current controller G_{pi}) works well under the speed step response.

F. Control Performance Under Parameter Error

Fig. 34 shows the experimental results of q-axis current step responses under parameter error of (a) $\hat{L} = 0.7L_{\text{norm}}$, (b) $\hat{C} = 0.7C_{\text{norm}}$, (c) $\hat{L} = 1.3L_{\text{norm}}$, and (d) $\hat{C} = 1.3C_{\text{norm}}$, in which L_{norm} and C_{norm} represent the normal values listed in Table I, and the estimated parameters $\hat{L}$ and $\hat{C}$ are used to calculate the control parameters of the proposed method. The HSPMSM speed is 12000 r/min (1000 Hz). It can be seen from Fig. 34 that the rise (or fall) times are in the range of 0.67–0.87ms (10–13 T), which is similar to the range of 0.6–0.8 ms (9–12 T) when parameters are accurate, as shown in Fig. 30(g)–(i). This indicates that the dynamic response speed is basically unchanged under the ±30% parameter error, which is consistent with the analysis in Fig. 22 that the dominant pole remains basically unchanged under the ±30% parameter error.

On the other hand, it can be seen from Fig. 34(a) ($\hat{L} = 0.7L_{\text{norm}}$) that, during the i_q step responses, the fluctuations of i_d are 0.3 A (10%) and 0.28 A (9.3%). It can be seen from Fig. 34(b) ($\hat{C} = 0.7C_{\text{norm}}$) that the fluctuations of i_d are 0.25 A

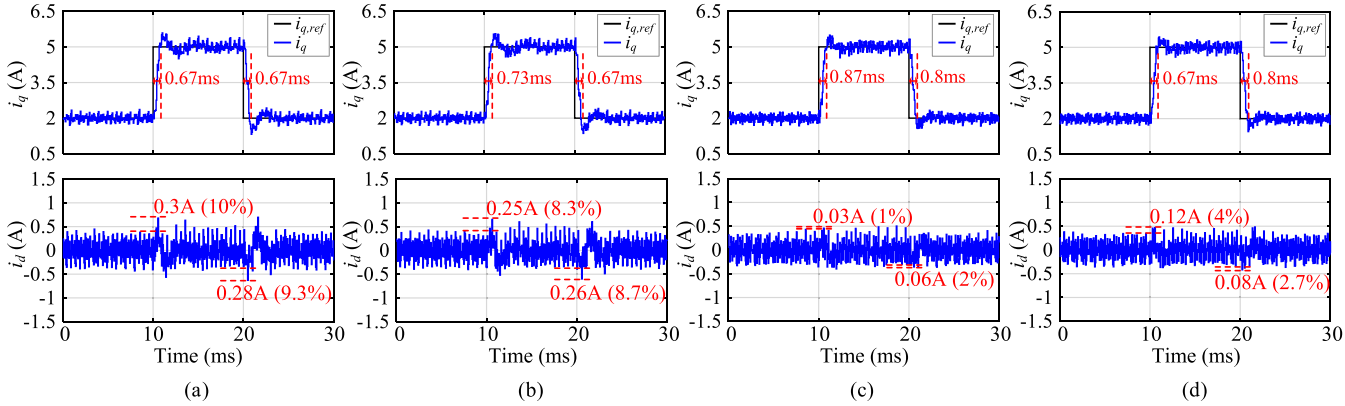

Fig. 34. Experimental results of q-axis current step responses at 12 000 r/min (1000 Hz) under parameter error. (a) $\hat{L} = 0.7L_{\text{norm}}$. (b) $\hat{C} = 0.7C_{\text{norm}}$. (c) $\hat{L} = 1.3L_{\text{norm}}$. (d) $\hat{C} = 1.3C_{\text{norm}}$.

(8.3%) and 0.26 A (8.7%). The above fluctuations of i_d are larger than those when the parameters are accurate, namely 0.15 A (5%) and 0.11 A (3.7%), as shown in Fig. 30(i). Meanwhile, it is observed from Fig. 34(a) and (b) that the trend of oscillatory appears after i_q step responses. Thus, there is certain deterioration in dynamic performance when the estimated parameters are relatively small.

In addition, Fig. 34(c) ($\hat{L} = 1.3L_{\text{norm}}$) shows that the fluctuations of i_d are 0.03 A (1%) and 0.06 A (2%). Fig. 34(d) ($\hat{C} = 1.3C_{\text{norm}}$) shows that the fluctuations of i_d are 0.12 A (4%) and 0.08 A (2.7%). The above fluctuations of i_d are smaller than that when the parameters are accurate, as shown in Fig. 30(c). This indicates that the dynamic decoupling performance remains good when the estimated parameters are relatively large. To sum up, the control performance will be affected to a certain extent under parameter errors. The control system remains stable under the $\pm 30\%$ error of $\hat{L}$ and $\hat{C}$, which verifies the parameter robustness of the proposed current control method.

VII. Conclusion

This article proposes a dynamic decoupling AD current control method for the CSI-fed HSPMSM drive with low carrier ratios. In the AD inner loop, the discrete-time-model-based MS-FAD is implemented to realize the desired resonance frequency and resonance pole modulus. Then, the LFETF-based dynamic decoupling controller is proposed to solve the serious cross coupling under low carrier ratios. On the above basis, an outer-loop PI controller is adopted to adjust the magnitude and phase of the open-loop transfer function. Theoretical analysis shows that the proposed current control method can achieve the desired open-loop cutoff frequency with enough PM and GM under the wide fundamental frequency changes of the HSPMSM, which ensures the dynamic performance, stability, and robustness of the system. The effectiveness of the proposed current control method is verified through experiments on a laboratory-scaled CSI-fed HSPMSM drive with the fundamental frequency of 1000 Hz and the carrier ratio of 15.

References

[1] D. Gerada, A. Mebarki, N. L. Brown, C. Gerada, A. Cavagnino, and A. Boglietti, "High-speed electrical machines: Technologies, trends, and developments," *IEEE Trans. Ind. Electron.*, vol. 61, no. 6, pp. 2946–2959, Jun. 2014, doi: 10.1109/TIE.2013.2286777.

[2] W. Deng and S. Zuo, "Electromagnetic vibration and noise of the permanent-magnet synchronous motors for electric vehicles: An overview," *IEEE Trans. Transp. Electrific.*, vol. 5, no. 1, pp. 59–70, Mar. 2019, doi: 10.1109/TTE.2018.2875481.

[3] K. Yamazaki and A. Abe, "Loss analysis of interior permanent magnet motors considering carrier harmonics and magnet eddy currents using 3-D FEM," in *Proc. IEEE Int. Electr. Mach. Drives Conf.*, 2007, vol. 2, pp. 904–909, doi: 10.1109/IEMDC.2007.382794.

[4] B. Wu, *High-Power Converters and AC Drives*. Hoboken, NJ, USA: Wiley/IEEE Press, 2006.

[5] J. I. Guzmán, J. R. Espinoza, L. A. Morán, and G. Joós, "Selective harmonic elimination in multimodule three-phase current-source converters," *IEEE Trans. Power Electron.*, vol. 25, no. 1, pp. 44–53, Jan. 2010, doi: 10.1109/TPEL.2009.2023658.

[6] V. Madonna, G. Migliazza, P. Giangrande, E. Lorenzani, G. Buticchi, and M. Galea, "The rebirth of the current source inverter: Advantages for aerospace motor design," *IEEE Ind. Electron. Mag.*, vol. 13, no. 4, pp. 65–76, Dec. 2019, doi: 10.1109/MIE.2019.2936319.

[7] B. Luckett, J. He, and X. Yuan, "Investigation of SiC current source inverter for medium-voltage high-frequency electric aircraft propulsion applications," in *Proc. IEEE 9th Int. Power Electron. Motion Control Conf. Asia*, 2020, pp. 3476–3481, doi: 10.1109/IPEMC-ECCEA-sia48364.2020.9367841.

[8] S. Yang, Z. Yin, C. Tong, Y. Sui, and P. Zheng, "Active damping current control for current-source inverter-based PMSM drives," *IEEE Trans. Ind. Electron.*, vol. 70, no. 4, pp. 3549–3560, Apr. 2023, doi: 10.1109/TIE.2022.3176270.

[9] L. Ding, Y. W. Li, and N. R. Zargari, "Discrete-time SMO sensorless control of current source converter-fed PMSM drives with low switching frequency," *IEEE Trans. Ind. Electron.*, vol. 68, no. 3, pp. 2120–2129, Mar. 2021, doi: 10.1109/TIE.2020.2972433.

[10] P. Liu et al., "Discrete-time complex-vector model based closed-loop current controller for CSC-fed PMAC machine systems with low carrier ratios," *IEEE Trans. Power Electron.*, vol. 38, no. 1, pp. 762–775, Jan. 2023, doi: 10.1109/TPEL.2022.3198075.

[11] S. Yang, C. Tong, Y. Sui, Z. Yin, and P. Zheng, "Current-source inverter fed five-phase PMSM drives with pentagon stator winding considering SVM scheme, resonance damping, and fault tolerance," *IEEE Trans. Ind. Electron.*, vol. 70, no. 6, pp. 5560–5570, Jun. 2023, doi: 10.1109/TIE.2022.3190848.

[12] Z. Wang, Y. Xu, P. Liu, Y. Zhang, and J. He, "Zero-voltage-switching current source inverter fed PMSM drives with reduced EMI," *IEEE Trans. Power Electron.*, vol. 36, no. 1, pp. 761–771, Jan. 2021, doi: 10.1109/TPEL.2020.3004633.

[13] M. A. Azghandi, S. M. Barakati, and A. Yazdani, "Passivity-based design of a fractional-order virtual capacitor for active damping of multiparalleled grid-connected current-source inverters," *IEEE Trans. Power Electron.*, vol. 37, no. 7, pp. 7809–7818, Jul. 2022, doi: 10.1109/TPEL.2022.3148242.

[14] Y. Geng, X. Song, X. Zhang, K. Yang, and H. Liu, "Stability analysis and key parameters design for grid-connected current-source inverter with capacitor-voltage feedback active damping," *IEEE Trans. Power Electron.*, vol. 36, no. 6, pp. 7097–7111, Jun. 2021, doi: 10.1109/TPEL.2020.3036187.

[15] C. Du, J. Zhou, and Y. Ma, "Predictive current control of a current-source inverter with active damping method," in *Proc. IEEE Energy Convers. Congr. Expo.*, 2015, pp. 1100–1104, doi: 10.1109/ECCE.2015.7309812.

[16] Z. Bai, H. Ma, D. Xu, B. Wu, Y. Fang, and Y. Yao, "Resonance damping and harmonic suppression for grid-connected current-source converter," *IEEE Trans. Ind. Electron.*, vol. 61, no. 7, pp. 3146–3154, Jul. 2014, doi: 10.1109/TIE.2013.2281173.

[17] M. Hinkkanen, H. Asad Ali Awan, Z. Qu, T. Tuovinen, and F. Briz, "Current control for synchronous motor drives: Direct discrete-time pole-placement design," *IEEE Trans. Ind. Appl.*, vol. 52, no. 2, pp. 1530–1541, Mar./Apr. 2016, doi: 10.1109/TIA.2015.2495288.

[18] H.-J. Lee, S. Jung, and S.-K. Sul, "A current controller design for current source inverter-fed AC machine drive system," *IEEE Trans. Power Electron.*, vol. 28, no. 3, pp. 1366–1381, Mar. 2013, doi: 10.1109/TPEL.2012.2208985.

[19] J. Zhang, Y. Huang, F. Peng, and Y. Yao, "Pole placement-based current control method for CSI-fed PMSM drive with eliminating capacitor voltage sampling," *IEEE Trans. Power Electron.*, vol. 38, no. 8, pp. 9409–9420, Aug. 2023, doi: 10.1109/TPEL.2023.3267075.

[20] S. Zhou, J. Liu, L. Zhou, and Y. Zhang, "DQ current control of voltage source converters with a decoupling method based on preprocessed reference current feed-forward," *IEEE Trans. Power Electron.*, vol. 32, no. 11, pp. 8904–8921, Nov. 2017, doi: 10.1109/TPEL.2017.2651139.

[21] R. A. Torres, H. Dai, W. Lee, T. M. Jahns, and B. Sarlioglu, "A simple and robust controller design for high-frequency WBG-based current-source-inverter-fed AC motor drive," in *Proc. IEEE Transp. Electrific. Conf. Expo.*, 2020, pp. 111–117, doi: 10.1109/ITEC48692.2020.9161527.

[22] B. Bahrani, S. Kenzelmann, and A. Rufer, "Multivariable-PI-based DQ current control of voltage source converters with superior axis decoupling capability," *IEEE Trans. Ind. Electron.*, vol. 58, no. 7, pp. 3016–3026, Jul. 2011, doi: 10.1109/TIE.2010.2070776.

[23] F. Briz, M. Degner, and R. Lorenz, "Analysis and design of current regulators using complex vectors," *IEEE Trans. Ind. Appl.*, vol. 36, no. 3, pp. 817–825, May/Jun. 2000, doi: 10.1109/28.845057.

[24] H. Kim, M. W. Degner, J. M. Guerrero, F. Briz, and R. D. Lorenz, "Discrete-time current regulator design for AC machine drives," *IEEE Trans. Ind. Appl.*, vol. 46, no. 4, pp. 1425–1435, Jul. 2010, doi: 10.1109/TIA.2010.2049628.

[25] F. Liu, B. Wu, N. R. Zargari, and M. Pande, "An active damping method using inductor-current feedback control for high-power PWM current-source rectifier," *IEEE Trans. Power Electron.*, vol. 26, no. 9, pp. 2580–2587, Sep. 2011, doi: 10.1109/TPEL.2011.2111423.

[26] Y. W. Li, B. Wu, N. R. Zargari, J. C. Wiseman, and D. Xu, "Damping of PWM current-source rectifier using a hybrid combination approach," *IEEE Trans. Power Electron.*, vol. 22, no. 4, pp. 1383–1393, Jul. 2007, doi: 10.1109/TPEL.2007.900499.

[27] W. Yao, Y. Yang, X. Zhang, F. Blaabjerg, and P. C. Loh, "Design and analysis of robust active damping for LCL filters using digital notch filters," *IEEE Trans. Power Electron.*, vol. 32, no. 3, pp. 2360–2375, Mar. 2017, doi: 10.1109/TPEL.2016.2565598.

[28] K. Hirano, S. Nishimura, and S. Mitra, "Design of digital notch filters," *IEEE Trans. Commun.*, vol. 22, no. 7, pp. 964–970, Jul. 1974, doi: 10.1109/TCOM.1974.1092311.

[29] N. Nain, S. Walser, J. Huber, K. K. Leong, and J. W. Kolar, "Self-reverse-blocking control of dual-gate monolithic bidirectional GaN switch with quasi-ohmic on-state characteristic," *IEEE Trans. Power Electron.*, vol. 37, no. 9, pp. 10091–10094, Sep. 2022, doi: 10.1109/TPEL.2022.3163589.

[30] A. Kanale, A. Agarwal, B. J. Baliga, and S. Bhattacharya, "Monolithic reverse blocking 1.2 kV 4H-SiC power transistor: A novel, single-chip, three-terminal device for current source inverter applications," *IEEE Trans. Power Electron.*, vol. 37, no. 9, pp. 10112–10116, Sep. 2022, doi: 10.1109/TPEL.2022.3166933.

Jindong Zhang (Student Member, IEEE) received the B.S. degree in electrical engineering in 2018 from Southeast University, Nanjing, China, where he is currently working toward the Doctor of Engineering in electric machines and control with the School of Electrical Engineering.

His main research interests include current control, position sensorless drive, and parameter identification of permanent magnet synchronous machine.

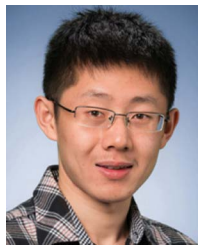

Fei Peng (Member, IEEE) received the B.S. and M.S. degrees in electrical engineering from Southeast University, Nanjing, China, in 2010 and 2012, respectively, and the Ph.D. degree in electrical and computer engineering from McMaster University, Hamilton, ON, Canada, in 2016.

He joined the School of Electrical Engineering, Southeast University, as an Assistant Professor. His research interests include optimal design and control of power converters, modeling, and digital control of motor drive.

Yunkai Huang received the M.Sc. and Ph.D. degrees in electrical engineering from Southeast University, Nanjing, China, in 2001 and 2007, respectively.

He is currently a Professor with the School of Electrical Engineering, Southeast University. His research interests include design and control of permanent magnet machine and high-speed machine, applications in domestic appliances, electric vehicles, railway traction, all-electric ships, more-electric aircraft, and wind power generation systems.

Yu Yao (Member, IEEE) received the B.S. degree in electrical engineering in 2016 from Southeast University, Nanjing, China, where he is currently working toward the Doctor of Engineering degree in electric machines and control with the School of Electrical Engineering.

His research interests include the design of power inverters, current regulator design, position sensorless drive for the high-speed permanent magnet synchronous machine, and active damping methods for the high-speed drive system with the LCL output filter.